40Ar diffusion in phlogopite: P V T atomistic calibration and implications for Ar–melt–solid kinetic interactions and ascent dynamics of mantle xenoliths and kimberlites

Jehiel Nteme, Stéphane Scaillet, Pascal Brault, Laurent Tassan-Got, Florian Duval

Geochimica et Cosmochimica Acta xxx (xxxx) xxx

Contents lists available at ScienceDirect

Geochimica et Cosmochimica Acta

journal homepage: www.elsevier.com/locate/gca

^{40}Ar diffusion in phlogopite: *PVT* atomistic calibration and implications for Ar–melt–solid kinetic interactions and ascent dynamics of mantle xenoliths and kimberlites

Jehiel Nteme [a,*], Stéphane Scaillet [b], Pascal Brault [a], Laurent Tassan-Got [c,d], Florian Duval [b]

[a] Univ. Orléans, CNRS, Groupe de Recherches sur l'Energétique des Milieux Ionisés (GREMI), UMR 7344, 45067 Orléans, France
[b] Univ. Orléans, CNRS, BRGM, Institut des Sciences de la Terre d'Orléans (ISTO), UMR 7327, F-45071, Orléans, France
[c] Université Paris-Saclay, CNRS, IN2P3, Laboratoire de Physique des deux infinis Irène Joliot-Curie (IJCLab), 91405 Orsay, France
[d] Conseil Européen pour la Recherche Nucléaire (CERN), Espl. des Particules 1, 1211 Meyrin, Geneva, Switzerland

ARTICLE INFO

Associate editor: Fred Jourdan

Dataset link: https://doi.org/10.5281/zenodo.10592905

Keywords:
^{40}Ar diffusion
Phlogopite
Molecular Dynamics
NEB
Mantle xenoliths
Ascent rates

ABSTRACT

^{40}Ar/^{39}Ar ages of phlogopite from kimberlite-hosted mantle xenoliths are commonly older than the kimberlite eruption, despite the fact that argon is supposed not to be retained by phlogopite at temperatures above hydrothermally-derived Ar closure temperatures (<500 °C). Combining Molecular Dynamics (MD) with Nudged Elastic Band (NEB) and Transition State Theory (TST), we investigate ^{40}Ar–*PVT* (Pressure–Volume–Temperature) relationships in pristine, defect-free, phlogopite and show that ^{40}Ar diffusivity is several orders of magnitude slower than existing estimates with a strong effect of pressure on diffusion rates and retention of ^{40}Ar at mantle conditions. These results imply to fundamentally revise residence- and transit-time estimates based on Ar kinetics in phlogopite assuming simple diffusive relaxation during upwelling. When accounting for pressure, ^{40}Ar retention trends in phlogopite predict substantially slower kimberlite ascent rates than documented by independent chronometers, indicating that ^{40}Ar resetting during ascent in phlogopite does not result from simple decompression-driven diffusive relaxation. We argue that ^{40}Ar remobilization probably involves secondary structural–textural modifications induced by reaction-driven recrystallization or rim overgrowth. These findings have far-reaching consequences in terms of argon isotopic mobility at mantle depths as well as for dating and tracing metasomatic events during crust–mantle interactions in the evolution of the subcontinental mantle.

1. Introduction

Phlogopite, the Mg–endmember of the trioctehadral mica series (Bailey, 1984), is a stable product of fluid–melt induced K/Mg–metasomatism, notably in mantle-derived (ultramafic) rocks. It is particularly abundant in kimberlites as a groundmass mineral (<100 μm), with occasional larger phenocrysts reaching sizes between 200–300 μm. It also occurs as xenocrystic or antecrystic macrocrysts (> 1 mm) included in mantle xenoliths or derived from disaggregation of mantle lithologies during kimberlite magma ascent (Mitchell, 1986; Reguir et al., 2009; Giuliani et al., 2016). Due to its high K content, it is commonly targeted for ^{40}Ar/^{39}Ar dating of mantle metasomatism and kimberlite-forming processes (Phillips, 1991; Kelley and Wartho, 2000; Wartho and Kelley, 2003; Hopp et al., 2008), as well as for tracing crust–mantle interactions and the evolution of the subcontinental mantle (Buikin et al., 2010).

However, ^{40}Ar/^{39}Ar dating of mantle phlogopites has proven challenging. While reliable ages have been obtained for phenocrystic phlogopite in kimberlites (e.g. Fitch and Miller, 1983; Allsopp and Roddick, 1984; Phillips et al., 1999), dating xenocrystic or antecrystic macrocrysts commonly results in complex Ar systematics with pronounced internal gradients in radiogenic Ar (hereafter ^{40}Ar*) or variably disturbed ^{40}Ar/^{39}Ar release patterns (Phillips and Onstott, 1986, 1988; Phillips, 1991; Kelley and Wartho, 2000; Wartho and Kelley, 2003; Hopp et al., 2008; Pokhilenko et al., 2013). Such complications often come along with ages up to 2 Gyr older than the inferred time of kimberlite emplacement, which have been ascribed to excess ^{40}Ar incorporation prior to or during ascent of the kimberlite melt into the crust (Kaneoka and Aoki, 1978; Phillips and Onstott, 1986, 1988; Phillips, 1991; Johnson and Phillips, 2003). Alternatively, some studies (e.g. Kelley and Wartho, 2000; Wartho and Kelley, 2003) have

* Corresponding author.
E-mail address: jehiel.nteme-mukonzo@univ-orleans.fr (J. Nteme).

https://doi.org/10.1016/j.gca.2024.07.008
Received 30 January 2024; Accepted 9 July 2024
Available online 22 July 2024

suggested that these older apparent ages could instead reflect primordial $^{40}Ar^{*}$ retention at temperatures up to ~700 °C, well in excess of the nominal closure temperature of ~480 °C inferred from early hydrothermal experiments (Giletti et al., 1974).

High–T ^{40}Ar retention in phlogopite has been attributed to the stable (equilibrium) incorporation of Ar due to the high Ar solubility in trioctahedral micas along with the preferred crystal/melt partitioning of K (±Ar) into the liquidus phlogopite phase at mantle depths (Foland, 1979; Dahl, 1996; Kelley and Wartho, 2000; Scibiorski et al., 2021). Vysotskii et al. (2011) instead suggested that high–T retention could result from strongly damped ^{40}Ar intracrystalline diffusivity at mantle pressures. Mixed hypotheses invoking both mechanisms (high affinity plus reduced diffusivity) have also been put forward to explain old core ages (up to 1.2 Ga) relative to the age of kimberlite emplacement in phlogopite from a large suite of peridotite xenoliths in South Africa and Lesotho (Hopp et al., 2008). Separately or in combination, both mechanisms imply that near–crystallization or metasomatic (trapping) ages may be retained by mantle phlogopite long before its entrainment and cooling through the crust (e.g., Pearson et al., 1997; Kelley and Wartho, 2000; Kempton et al., 2001; Wartho and Kelley, 2003).

Such uncertainties in terms of excess (unsupported) *vs.* radiogenic (closed-system) origin stem in part from the complex fluid–melt–solid interactions and metasomatic processes affecting the source regions sampled by kimberlite melts. They also reflect our limited understanding of the K/Ar behavior of mantle phases. In the case of phlogopite, much is unknown of its Ar retention properties at the unusually extreme conditions (and strong pressure changes) experienced during crystallization and ascent from mantle depths. The only available diffusivity estimates so far derive from quite old or limited hydrothermal experimental data (Giletti et al., 1974; Giletti and Tullis, 1977; Yudin et al., 2021).

From recent field and theoretical studies, it is increasingly recognized that hydrothermal experiments can considerably overestimate the natural diffusivity of ^{40}Ar in micas. Preparatory steps such as mechanical grinding used to extract natural crystals or reduce their grain size (to optimize fractional exchange and loss) may artificially enhance the bulk diffusivity by introducing microstructural defects acting as high-diffusivity pathways during heating experiments (Dunlap, 1997). Also, the growth of interlayer secondary phases (Onstott et al., 1991) and dissolution–precipitation reactions may occur with the fluid–confining medium (Hammouda and Cherniak, 2000), adversely affecting the mica stability and its intrinsic diffusive properties during hydrothermal heating. Such shortcomings have been invoked to explain drastic differences between hydrothermal experiments and theoretical ^{40}Ar diffusion rates predicted by atomistic modeling in white mica (Nteme et al., 2022, 2023). Because of the strong similarity in crystal structure between muscovite and phlogopite, similar limitations likely apply to hydrothermally-derived ^{40}Ar data from phlogopite as well.

Establishing the kinetic and retention properties of ^{40}Ar in phlogopite and their dependence on intensive $P-T$ variables is crucial for two reasons. First, the genetic significance of anomalous $^{40}Ar/^{39}Ar$ ages from mantle phlogopite in kimberlites must be cleared out to properly constrain both the residence time and ascent dynamics of metasomatized xenoliths and their host kimberlites in the sub-continental mantle. Next, such retention properties have far-reaching implications in terms of storage capacity of phlogopite for volatiles and noble gases residing in the mantle. Solubility studies suggest that noble gases are hosted in the mica interlayer, either interstitially or in unoccupied ring structures, allowing them – notably phlogopite – to sequester and transport volatiles deep into the mantle (Jackson et al., 2015). These characteristics make them unique for tracing mantle–fluid dynamics using noble gases trapped or recycled in hydrous mantle phases (Buikin et al., 2010; Wang et al., 2020), but have not been properly calibrated yet.

This study is a fresh attempt at constraining ^{40}Ar diffusion rates in phlogopite from first-order (crystal-based) kinetic modeling as done before for white mica (Nteme et al., 2022, 2023). Such a theoretical approach permits to investigate ^{40}Ar diffusive behavior at the atomic scale in a defect-free and stœchiometrically stable lattice structure, avoiding the issues of mica stability and microstructural defects during laboratory heating of natural specimens. By combining Molecular Dynamics (MD) with Transition State theory (TST), we re-evaluate ^{40}Ar diffusivity in phlogopite and its dependence to both temperature and pressure. Our results show that ^{40}Ar diffusion kinetics are orders of magnitude slower than previous estimates with a strong dependence on confining pressure. These results provide the first physically-grounded framework for benchmarking pressure effects operating in sheet silicates during protracted residence at mantle conditions, allowing the reassessment of the potential of phlogopite for preserving mantle-derived $^{40}Ar-$ isotopic signatures and for tracking time-kinetic processes during kimberlite formation and ascent.

2. Model and methods

2.1. Crystal structure model

Phlogopite [$KMg_3(Si_3Al)O_{10}(OH)_2$] has a layered structure composed of a stacking of tetrahedral (T) silicate and octahedral (O) magnesian layers forming T–O–T structures. These are held together by interlayer K^+ ions which compensate the negative structural charge resulting from the substitution of Al for Si (Bailey, 1984). The phlogopite atomic model used in this study (Fig. 1a) is taken from the experimental data of Brigatti and Davoli (1990). A periodic supercell of size $6 \times 3 \times 2$ was built by expanding the unit cell in the corresponding a, b, c crystallographic directions, respectively. Tetrahedral Al atoms were distributed in an irregular pattern. Consistent with the Lowenstein's rule (Loewenstein, 1954), no single basal oxygen was allowed to bridge two tetrahedral aluminium atoms (Fig. 1b). Interlayer K^+ ions were located between one Si_5Al_1 ring and one Si_4Al_2 ring to ensure a local charge equilibrium (Herrero et al., 1987, 1985).

2.2. Model implementation

Classical Molecular Dynamics (MD) involves simulating the trajectory of a system composed of interacting particles, such as atoms and/or molecules, over time by solving Newton's equations of motion (Frenkel and Smit, 2002; Rapaport, 2004). Atomic interactions are calculated using force fields, which are parameterized using either experimental data or *ab initio* simulations. MD simulations were conducted using the LAMMPS simulation package (Thompson et al., 2022) and the ClayFF force field (Cygan et al., 2004). The latter is a flexible model that computes pairwise energies of atoms in hydrated mineral systems through nonbonded electrostatic and Lennard-Jones terms (except for interactions between hydroxyl atoms that are described by a simple harmonic term). Interaction parameters used in this study are reported in Table 1. Since partial charges in the original ClayFF model were derived for dioctahedral structures, a modification of the charges of oxygens bridging octahedral cations in the trioctahedral phyllosilicates is required to ensure neutrality. While some authors modify only the partial charge of apical oxygens (e.g., Du and Miller, 2007), we have distributed the excess charge evenly between all oxygens bridging octahedral cations, including oxygens of the hydroxyl group. Ar was assigned a zero charge and Lennard-Jones parameters (σ and ϵ) from White (1999).

The phlogopite atomic model was optimized via 250 ps simulations performed in the isobaric–isothermal (NPT) ensemble using the Nosé–Hoover thermostat and barostat, with relaxation times of 0.01 and 1 ps, respectively, and a time step of 0.001 ps. Long-range interactions were treated using the Ewald summation whereas short-range interactions were evaluated with a cut-off distance of 10 Å. Migration energy barriers were computed using the Nudged Elastic Band (NEB) method (Jónsson et al., 1998). The latter calculates the Minimum Energy Path

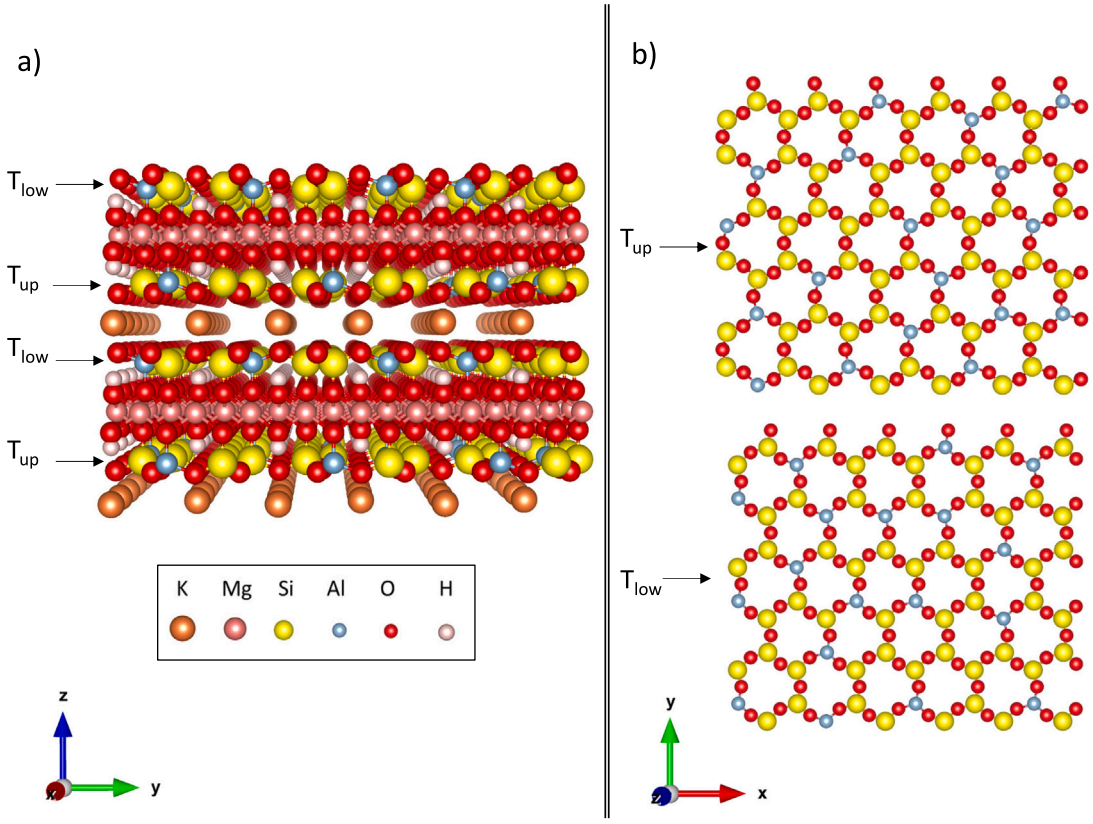

Fig. 1. Crystal structure atomic model of phlogopite imaged with VESTA (Momma and Izumi, 2011). The system (n = 1584 atoms) consists of a supercell (6 × 3 × 2 unit cells) of initial dimensions L_x = 32.058 Å, L_y = 27.774 Å and L_z = 20.453999 Å. (a) Perspective view down the a axis. (b) Tetrahedral layers (as labeled in (a)) showing the irregular distribution of Al atoms. Atoms drawn with their Van der Waals radii. T_{up} and T_{low} indicate the upper and the lower tetrahedral layers with respect to the interlayer region, respectively.

Table 1
Interaction parameters used in the simulations.

Nonbonded parameters			
Atoms	Charge (e)	σ (Å)	ϵ (kcal mol^{-1})
H (hydroxyl)[a]	0.4250	–	–
O1 (hydroxyl)[a]	−1.1050	3.1655	0.1554
O2 (bridging Oxygen)[a]	−1.0500	3.1655	0.1554
O3 (bridging Oxygen bonded to Al)[a]	−1.1688	3.1655	0.1554
O4 (Oxygen bonded to Mg)[a]	−1.2050	3.1655	0.1554
O5 (Oxygen bonded to both Mg and Al)[a]	−1.32375	3.1655	0.1554
Mg[a]	1.3600	5.2643	9.0298 × 10^{-7}
Al (tetrahedral)[a]	1.5750	3.3020	1.8405 × 10^{-6}
Si[a]	2.1000	3.3020	1.8405 × 10^{-6}
K[a]	1.0000	3.3340	0.1000
Ar[b]	0.0000	3.4010	0.2304
Bonded parameters			
Atom 1	Atom 2	k_1 (kcal mol^{-1} Å^{-2})	r_0 (Å)
O1 (hydroxyl)	H (hydroxyl)	554.1349	1.0000

[a] Cygan et al. (2004).
[b] White (1999).

(MEP) by solving independent system images (= intermediate transition states), each containing one ^{40}Ar atom between stable sites. The migration energy is derived from the difference between the saddle point and the initial site energy. Diffusion rates based on these barriers were evaluated using Transition State Theory (further details may be found in Nteme et al. (2022)). The effect of pressure on ^{40}Ar diffusion was investigated using a constant volume approach (Karki and Khanduja, 2006; Ammann et al., 2009). Pressure–Volume relationships were obtained by equilibrating the system at the desired pressures via NPT simulations. At each pressure, the optimized volume of the system was kept fixed and only the internal energy was set free in the calculation of the migration barriers.

Before simulating Ar diffusion, we tested the suitability of ClayFF for modeling structural properties of phlogopite. We compared the lattice parameters computed at ambient conditions (P = 0.001 kbar and T = 25 °C) for our phlogopite atomic model with experimental data of Brigatti and Davoli (1990). The results (Table 2) reveal that ClayFF reproduces the experimental crystal structure fairly well, with the lattice parameters a, b, c, the angles α, β, γ and the interlayer separation all within 2 % of the experimental values. The stacking structure of T–O–T layers is also well reproduced. In the interlayer region, the basal

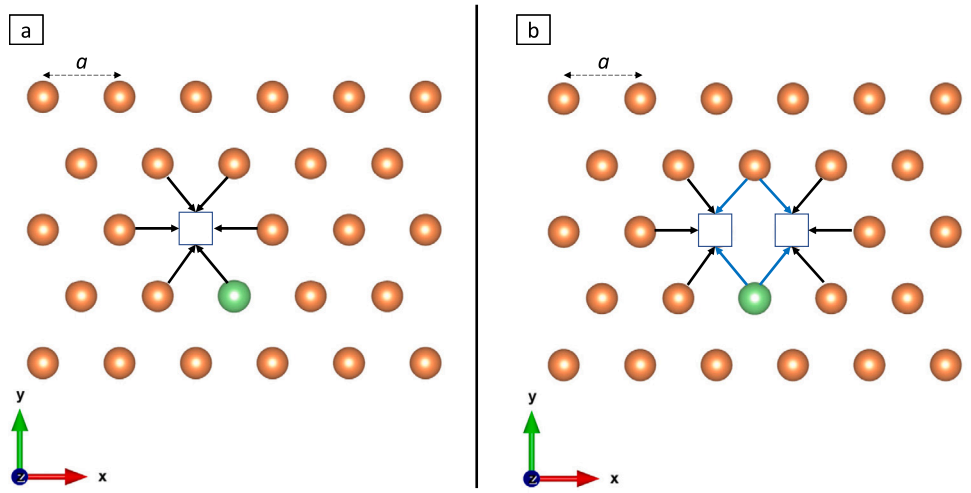

Fig. 2. Geometry of diffusion along the phlogopite interlayer. (a) Monovacancy mechanism. (b) Divacancy mechanism. Orange and green circles correspond to K^+ and ^{40}Ar atoms respectively.

Table 2
Comparison of experimental and simulated crystallographic parameters of 1*M* phlogopite.

	Experiment	MD simulations (ClayFF)	Deviation (± %)
a (Å)	5.343	5.247	−1.83
b (Å)	9.258	9.093	−1.81
c (Å)	10.227	10.134	−0.92
α (°)	90.000	90.069	+0.08
β (°)	100.260	100.457	+0.20
γ (°)	90.000	89.914	−0.10
Interlayer sep. (Å)	3.391	3.439	+1.40

oxygens of one T–O–T layer are directly above those of the adjacent layer and each potassium atom resides at the center of the upper and lower tetrahedral rings. In keeping with experimental data, the hydroxyl groups point normal to the (001) plane. Such congruence of MD predictions with empirical crystal-structural data provides independent validation of the force-field used, and independent evidence that the structure modeled is realistic.

3. Diffusion pathways and ^{40}Ar migration barriers

3.1. Diffusion pathways

Phlogopite is structurally similar to muscovite, the main difference being the full occupancy of octahedral sites (by Mg) and the orientation of hydroxyl groups pointing towards the interlayer region in phlogopite. Accordingly, most of the conclusions drawn from the study of ^{40}Ar diffusion in muscovite (Nteme et al., 2022) also apply to phlogopite. For example, MD simulations of ^{40}Ar recoil in phlogopite show that ^{40}Ar remains near its production site and resides essentially in a regular interlayer site, as previously reported in muscovite and illite (Szczerba et al., 2015; Nteme et al., 2022). Furthermore, the incorporation of ^{40}Ar into an interlayer interstitial site causes important distortions of the structure and increases the total energy of the system by ~90 kcal mol^{-1}. As discussed for muscovite (Nteme et al., 2022), this is a highly unfavorable configuration energetically which precludes protracted ^{40}Ar residence in the interstitial site and rules out interstitial diffusion as a viable mechanism for ^{40}Ar transport in phyllosilicates on geologic timescales.

To explore the alternative (vacancy) mechanism, we introduced interlayer vacancies in our phlogopite model and performed MD simulations in the NPT ensemble at temperatures up to 1000 °C and $P < 5$ kbar, for time durations up to 25 ns. In keeping with ^{40}Ar diffusion in muscovite, no migration of ^{40}Ar or K^+ could be observed, confirming the infrequent success of jumps into interlayer vacancies on timescales of classical MD. To circumvent this timescale limitation, we used the NEB method to determine the migration barriers for ^{40}Ar jumps to neighboring vacancies and Transition State Theory (TST) to compute the associated diffusion coefficients. The migration barriers were computed in a phologopite model equilibrated via NPT simulations at $T = 0.5$ K and $P = 0$ kbar. Since the motion of K^+ is required for a vacancy to get close to ^{40}Ar, we also computed the energy barriers associated with the migration of K^+ atoms. As for muscovite Nteme et al. (2022), we considered both the monovacancy and the divacancy mechanisms (Fig. 2). Because of the irregular distribution of Al atoms in the tetrahedral layers, we positioned ^{40}Ar and K^+ at each interlayer site of the model and computed the migrations energies towards all possible neighboring sites. The total possible combinations amount to 216 barriers for the monovacancy mechanism and 432 barriers for divacancy mechanism. The latter refers only to the “blue” jumps in Fig. 2b since the migration barriers related to the “black” jumps are identical to those computed for the monovacancy mechanism (Nteme et al., 2022).

3.2. ^{40}Ar migration barriers

The migration barriers associated with vacancy diffusion are characterized by mean values of 82 ± 3 kcal mol^{-1} (1σ) for the monovacancy mechanism and 79 ± 3 kcal mol^{-1} (1σ) for the divacancy mechanism (Fig. 3a, b). They are qualitatively similar to the behavior observed in muscovite (Nteme et al., 2022) with the energy barrier being slightly higher for the monovacancy mechanism (Fig. 3c). For each jump, the forward and backward migration barriers are similar. Likewise, ^{40}Ar follows the same rectilinear path towards a single vacancy, and a slightly curvilinear trajectory towards a vacancy pair (Fig. 3d). Similarly, the computed barriers are anti-correlated to the electrostatic energy, the highest barriers corresponding to migration paths interacting with the most closest-neighboring Si atoms (Fig. 3e).

Despite these similarities, differences are also seen between the two minerals. While ^{40}Ar migration barriers are distributed in both minerals, the dispersion is less pronounced in phlogopite. Furthermore, the migration barriers are significantly higher in phlogopite than in muscovite. These differences reflect the different octahedral occupancy between both minerals. In muscovite, the migration barrier is modulated by the irregular distribution of tetrahedral Al, but also by the relative position (and flexibility) of the octahedral vacancy with respect to the migration path (Nteme et al., 2022). In phlogopite, the

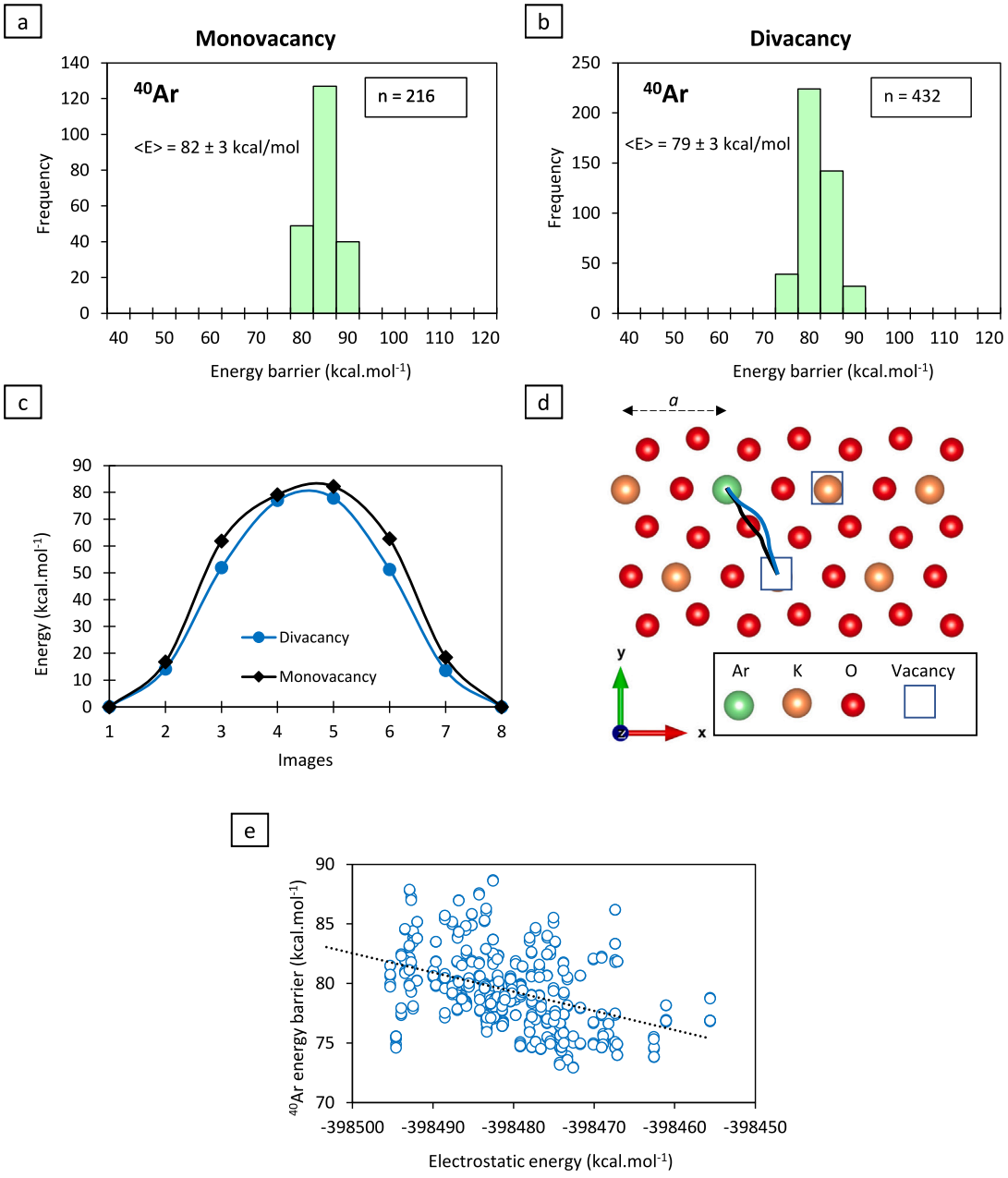

Fig. 3. NEB modeling of ^{40}Ar migration in phlogopite. (a) Histogram of migration barriers for the monovacancy mechanism. (b) Histogram of migration barriers for the divacancy mechanism. (c) Variation of the potential energy of ^{40}Ar along its path towards a monovacancy (black) and a vacancy pair (blue). (d) ^{40}Ar trajectory from a stable site towards a single vacancy (black) or a vacancy pair (blue). Red circles are basal oxygens. e) Anticorrelation between the ^{40}Ar migration barriers and the total electrostatic energy of the structure.

latter effect is suppressed by the full occupancy of the octahedral sites (by Mg). On its way towards a vacancy, ^{40}Ar in both minerals must pass directly between two basal oxygens facing each other (Fig. 3d). These must move apart normal to the migration path to facilitate the ^{40}Ar jump, a modification also involving the tetrahedra to which they belong. In muscovite, the displacement of tetrahedra normal to (001) is accommodated by the motion of octahedral Al towards the octahedral vacancy. In phlogopite, such a collective displacement normal to (001) cannot be accommodated in the octahedral layer, thus increasing the energy threshold required for ^{40}Ar to get past the two basal oxygens.

3.3. K^+ migration barriers

As for ^{40}Ar, the energy barriers for K^+ migration towards neighboring vacancies are distributed (Fig. 4a, b) with mean values of 71 ± 7 kcal mol^{-1} (1σ, mono-vacancy) and 59 ± 11 kcal mol^{-1} (1σ, divacancy). The energy landscape is much like in muscovite: (*i*) the K^+ energy barrier for the same path is significantly lower for the divacancy mechanism (Fig. 4c), (*ii*) the forward and the backward barriers are slightly different (Fig. 4c), (*iii*) potassium follows a curvilinear path from its stable site to a vacancy (Fig. 4d), and (*iv*) the K^+ migration barriers are positively correlated to ^{40}Ar migration barriers (Fig. 4e). The main difference is the significantly lower K^+ migration barriers in phlogopite compared to muscovite. Also, the mean barrier to K^+ jumping into single vacancies is lower than for ^{40}Ar (it is the reverse in muscovite). Such difference between K^+ and ^{40}Ar relates to differences in trajectories towards neighboring vacancies. As discussed above, the ^{40}Ar crossing between opposite basal oxygens is energetically involved (to overcome the lack of tetrahedra flexibility normal to (001) in phlogopite). Potassium follows a distinct path avoiding this configuration,

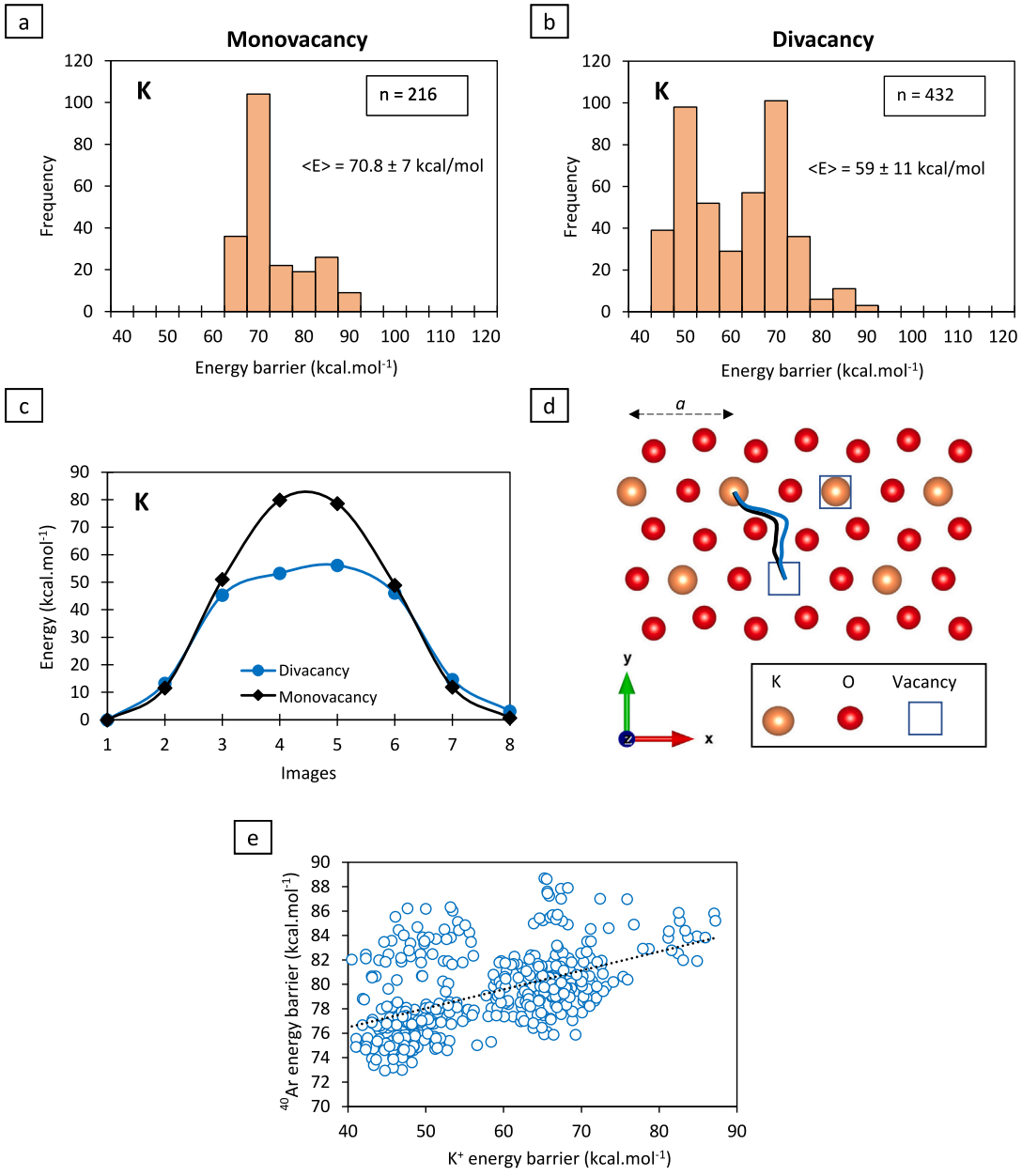

Fig. 4. NEB modeling of K^+ migration in phlogopite. (a) Histogram of migration barriers for the monovacancy mechanism. (b) Histogram of migration barriers for the divacancy mechanism. (c) Variation of the potential energy of K^+ along its path towards a monovacancy (black) or a vacancy pair (blue). (d) K^+ trajectories from a stable site towards a single vacancy (black) and a vacancy pair (blue). Red circles are basal oxygens. (e) Correlation diagram between ^{40}Ar and K^+ migration barriers.

thus requiring relatively less energy to complete a successful jump. K^+ barriers are also affected by the orientation of OH groups. The latter point towards the interlayer region, causing a repulsion between H^+ and K^+. This weakens the attractive force between K^+ and the basal oxygens, thus making potassium more mobile (Dahl, 1996; Dahl and Dorais, 1996). The effect of OH groups on K^+ barriers disappears when OH is completely substituted by F. In this case, the migration barrier of K^+ becomes similar to that of muscovite (Nteme, 2021).

4. Temperature dependence of ^{40}Ar diffusion

From TST, the diffusion coefficient is thermodynamically related to the jump frequency through:

$$D = ga^2\gamma \tag{1}$$

where g is a numerical constant depending on lattice geometry, a is the distance between two neighboring lattice sites and γ the jump probability given by:

$$\gamma = \nu \exp\left(-\frac{E}{RT}\right) \tag{2}$$

where ν is the attempt frequency (commonly approximated by the lattice Debye frequency, typically between 10^{12} and 10^{13} Hz), E the migration barrier (enthalpy of motion), R the gas constant, and T the temperature of the system (in Kelvin). Combining Eqs. (1) and (2) yields the classic Arrhenian form

$$D = D_0 \exp\left(-\frac{E}{RT}\right) \tag{3}$$

with $D_0 = ga^2\nu$ encapsulating the pre-exponential structural –vibrational frequency factor.

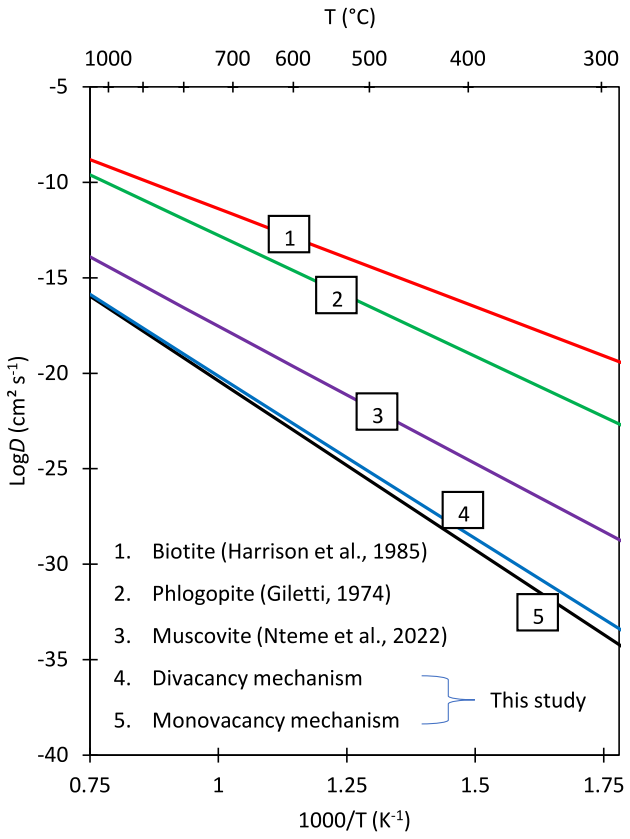

Fig. 5. Arrhenius plot of ^{40}Ar diffusion coefficients calculated for the monovacancy and the divacancy mechanisms. Results of previous studies (including muscovite and biotite) are also reported for comparison.

Eqs. (3) and (1) provide the physical-atomistic basis to compute the diffusion coefficient in a crystal where the migration barrier is the same for all equivalent jumps in an isotropic lattice. As discussed elsewhere (Nteme et al., 2022), because of the irregular distribution of Al atoms in the tetrahedral layers, the energy barrier for atoms moving in the interlayer region (a 2D lattice with hexagonal symmetry) varies from one direction to another, and from one interlayer site to another. This crystal-structural dependence is taken into account by considering an overall effective migration energy for each diffusing atom, E_{eff}, defined as:

$$\exp\left(\frac{E_{\text{eff}}}{RT}\right) = \frac{1}{n}\sum_{i=1}^{n}\exp\left(\frac{E_i}{RT}\right) \tag{4}$$

where E_i is the energy barrier required for an atom to leave an interlayer site i and n is the total number of stable sites in the interlayer region. The effective energy barrier for each site is derived from:

$$\exp\left(-\frac{E_i}{RT}\right) = \frac{1}{m}\sum_{j=1}^{m}\exp\left(-\frac{E_{ij}}{RT}\right) \tag{5}$$

in which E_{ij} is the migration energy for leaving the interlayer site i in the direction j, and m is the number of all possible directions ($m = 6$ in a hexagonal lattice). Using the energy barriers calculated above and the same notation for vacancy-mediated motion as in Nteme et al. (2022), the calculated effective ^{40}Ar migration energy barriers are $E_{\text{eff}}^{\text{Ar}\square} = 81$ kcal mol^{-1} (monovacancy mechanism) and $E_{\text{eff}}^{\text{Ar}\square\square} = 77$ kcal mol^{-1} (divacancy mechanism). For K$^+$ (or vacancy) migration, the effective barriers are $E_{\text{eff}}^{\text{K}\square} = 67$ kcal mol^{-1} (monovacancy mechanism) and $E_{\text{eff}}^{\text{K}\square\square} = 49$ kcal mol^{-1} (divacancy mechanism).

4.1. Diffusion coefficient for the monovacancy mechanism

As mentioned above, the migration of ^{40}Ar via the vacancy mechanism requires the motion of K$^+$ atoms to allow a vacancy to get close to ^{40}Ar. NEB calculations above show that the ^{40}Ar effective migration barrier associated with the monovacancy mechanism in phlogopite is higher than that of K$^+$, unlike muscovite where the opposite occurs. Therefore, the ^{40}Ar ⇆ □ oscillations described in muscovite will not occur in phlogopite and a vacancy available next to ^{40}Ar will be preferentially filled by K$^+$. The success rate for ^{40}Ar jumping into the vacancy instead of K$^+$ is thus lower and governed by the net diffusion coefficient (Nteme, 2021):

$$D_{\text{Ar}\square} = \frac{3}{2}a^2\nu\rho\exp\left(-\frac{E_{\text{eff}}^{\text{Ar}\square}}{RT}\right) \tag{6}$$

Assuming the standard values $\nu = 5\times10^{12}$ s^{-1}, $\rho = 0.1$ (the fraction of interlayer vacancies) and $a = 5.3$ Å, this translates into $D_{\text{Ar}\square} = 1.4\times10^{-22}$ cm^2 s^{-1} at $T = 700$ °C, a diffusion coefficient two orders of magnitude lower than for muscovite (Nteme et al., 2022).

4.2. Diffusion coefficient for the divacancy mechanism

In the divacancy mechanism, the diffusing atom can be adjacent to either one or both vacancies of the vacancy pair (Fig. 2b). In the latter configuration, the migration barriers are lower. This ensures the correlated mobility of divacancies along the interlayer region. As for muscovite, NEB calculations show that the ^{40}Ar effective migration barrier in the divacancy case is higher than for K$^+$. Accordingly, the ^{40}Ar diffusion coefficient is equally calculated via (Nteme et al., 2022):

$$D_{\text{Ar}\square\square} = \frac{5}{2}\rho^2a^2\nu\left[3\exp\left(-\frac{E_{\text{eff}}^{\text{Ar}\square}}{RT}\right)+\exp\left(-\frac{E_{\text{eff}}^{\text{Ar}\square\square}}{RT}\right)\right] \tag{7}$$

At $T = 700$ °C and $\rho = 0.1$, ^{40}Ar diffusivity via the divacancy mechanism is $D_{\text{Ar}\square\square} = 2.04\times10^{-21}$ cm^2 s^{-1}. This is one order of magnitude greater than for the monovacancy mechanism but three orders of magnitude lower than the corresponding mechanism in muscovite (Nteme et al., 2022). ^{40}Ar diffusion is therefore described by the Arrhenius parameters $E = 77$ kcal mol^{-1} and $D_0 = 6\times10^{-4}$ cm^2 s^{-1} (Fig. 5). A summary listing of the final estimates is provided in Table 3.

5. Pressure effect

Among the parameters most likely to play a role in ^{40}Ar diffusion at mantle pressure is the activation volume, i.e., the extra strain-electrostatic work done by a diffusing atom to overcome the reduction in lattice spacing (and increase in energy barrier) due to elastic compressibility and stiffness (the shear modulus of the crystal–elastic tensor). Experimental data in this connection are scarce and contradictory. Early experiments performed at 900 °C, 1080 °C, and 15 kbar (Giletti and Tullis, 1977) initially appeared to negate a significant pressure effect by indicating ^{40}Ar diffusion rates similar to those found at 2 kbar (Giletti et al., 1974), though a reduction in diffusivity was actually found at 900 °C. Later on, an activation volume of 14 cm^3 mol^{-1} was experimentally derived for biotite (Harrison et al., 1985) and muscovite (Harrison et al., 2009) via high-pressure hydrothermal runs at 14 kbar for biotite and 20 kbar for muscovite, implying a sizable effect on ^{40}Ar mobility in micas. A similar (or even greater) effect is to be expected in phlogopite that displays pronounced elastic strain anisotropy (Chheda et al., 2014), which has not been evaluated yet in terms of diffusivity.

The Arrhenius equation modified to account for the pressure effect reads:

$$D = D_0\exp\left(-\frac{E+P\Delta V}{RT}\right) \tag{8}$$

Table 3
Computed migration barriers and ^{40}Ar diffusion parameters for the monovacancy (□) and divacancy (□□) mechanisms.

Mechanism	Mean energy barriers		Effective energy barriers		^{40}Ar Diffusion parameters	
	$\langle E^{Ar} \rangle$ (kcal mol^{-1})	$\langle E^{K} \rangle$ (kcal mol^{-1})	E_{eff}^{Ar} (kcal mol^{-1})	E_{eff}^{K} (kcal mol^{-1})	E (kcal mol^{-1})	D_0 (cm^2 s^{-1})
□	82 ± 3	71 ± 7	81	67	81	2×10^{-3}
□□	79 ± 3	59 ± 11	77	49	77	6×10^{-4}

Table 4
Pressure dependence of structural parameters and migration barriers of ^{40}Ar in phlogopite.

P (kbar)	0	10	20	30	40	50
Lattice parameters						
a (Å)	5.231	5.222	5.215	5.207	5.194	5.184
b (Å)	9.065	9.050	9.036	9.023	8.998	8.979
c (Å)	20.121	19.834	19.621	19.448	19.343	19.232
α (°)	89.563	89.807	89.890	90.036	89.887	89.858
β (°)	100.747	100.506	100.551	100.585	100.535	100.553
γ (°)	90.005	89.996	89.997	89.984	89.990	89.983
Vol (Å^3)	937.365	921.668	908.888	898.150	899.408	891.016
Interlayer sep. (Å)	3.387	3.267	3.177	3.105	3.062	3.018
Migration barriers						
$E_{eff}^{Ar□}$ (kcal mol^{-1})	81	93	105	115	123.3	130.5
$E_{eff}^{Ar□□}$ (kcal mol^{-1})	77	91	103	114	121.6	128.6

where the activation volume ΔV for the diffusing species is approximated as:

$$\Delta V \approx -RT\left(\frac{\partial \ln D}{\partial P}\right)_T \quad (9)$$

where the logarithmic derivative of the vibrational term has been neglected (Mehrer, 2007).

In the spirit of checking the pertinence of our atomic-electrostatic model for describing the structural behavior of phlogopite at mantle depths, we first investigated the lattice parameters predicted at high−P by ClayFF and confronted the calculations with available compressibility-structural data before investigating the effect of pressure on ^{40}Ar migration. To this end, we equilibrated the phlogopite crystal via NPT simulations at room temperature and pressures ranging from 0 to 50 kbar using the same model setup as above.

Our simulations show that compressibility along the three crystallographic axes a, b, and c is linear and strongly anisotropic across the considered pressure range (Table 4). The results are closely consistent with experimental and DFT data (e.g., Hazen and Finger, 1978; Pavese et al., 2003; Comodi et al., 2004; Hernández-Laguna et al., 2019), underscoring the fact the phyllosilicate structure is softer along the c axis which corresponds to the direction involving the weakest bonds and electrostatic repulsive forces across the interlayer region (Fig. 6). Such a good agreement lends confidence that ClayFF accurately predicts the mica lattice properties in the range investigated, legitimating its use for exploring ^{40}Ar diffusivity at mantle pressures.

The pressure effect on ^{40}Ar diffusion was investigated by NEB simulations of the ^{40}Ar migration energies in a phlogopite structure equilibrated at T = 0.5 K across the pressure range considered above. Our results reveal a significant pressure effect on the ^{40}Ar migration barrier (Table 4). Note that elastic relaxation effects on the enthalpy $E_{eff}^{Ar□□}$ (divacancy-mediated diffusion) are not strictly linear but level off slightly as the pressure increases (Fig. 7). In the linear approximation, the increase is about 1 cal mol^{-1}.bar^{-1} from 77 kcal mol^{-1} (0 kbar) to 128 kcal mol^{-1} (50 kbar) (and approximately by the same coefficient for the monovacancy mechanism), corresponding to an activation volume of 42 cm^3 mol^{-1}. This is substantially greater than previous estimates ~14 cm^3 mol^{-1} for other micas (Harrison et al., 1985, 2009). Incidentally, a similar pressure dependence was quantified via DFT in lizardite by Wang et al. (2020) who identified a similar increase around 0.8 cal mol^{-1}.bar^{-1} for the enthalpy of ^{40}Ar motion in this phyllosilicate structurally similar to phlogopite (e.g., Sharp et al., 1990). Such a strong pressure effect on ^{40}Ar diffusion appears to be the rule for all phyllosilicates as a result of the preferential compressibility along the c axis and the collapse induced across the interlayer region where diffusion takes place (with up to −10 % reduction in interlayer spacing from 0 to 50 kbar in phlogopite, Table 4, Fig. 7).

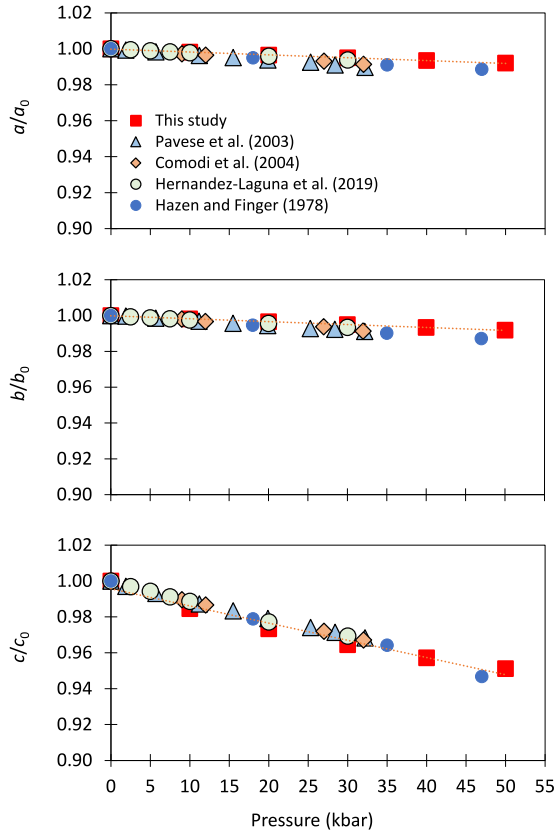

Fig. 6. Variations in lattice parameters of phlogopite as a function of pressure. Note the good agreement between ClayFF predictions and the results of Hazen and Finger (1978), Pavese et al. (2003), Comodi et al. (2004), Hernández-Laguna et al. (2019).

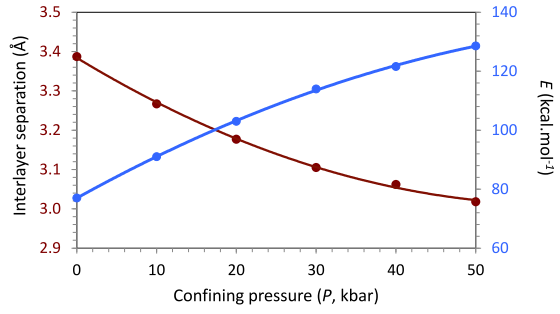

Fig. 7. Pressure effect on both the interlayer region and the ^{40}Ar migration barriers. Note the perfect symmetry between both curves.

6. Discussion

6.1. Ar diffusion structure of phlogopite

Our MD + NEB simulations are the first of their kind to investigate structural-electrostatic interactions with Ar diffusion in phlogopite, providing considerable insights into atomic-scale processes and associated crystallographic factors governing Ar motion in the interlayer region, the path of Ar preferential transfer in micas (Nteme et al., 2022). Our results show that, in terms of crystal strain-electrostatic considerations, Ar diffusion is extremely sluggish in an ideal, defect-free, phlogopite structure, and substantially much slower than in muscovite (Fig. 5). In particular, our results predict ^{40}Ar diffusivities in phlogopite several orders of magnitude lower than that reported in hydrothermal experiments, including biotite (up to 8 orders of magnitude difference at 700 °C; Fig. 5).

A similar diffusivity contrast between hydrothermal experiments and atomistic simulations has been found in white mica (Nteme et al., 2022). Using high-resolution ^{40}Ar/^{39}Ar mapping along (001) in slowly cooled muscovite, it was shown that this difference was the result of extended defects enhancing net transport rates in natural mica by to up seven orders of magnitude above theoretical MD + NEB estimates (Nteme et al., 2023). These defects were identified in the form of lenticular voids and basal partings, <100 nm–long, distributed in crystal zones affected by anomalously rapid diffusion with a boost factor $\psi_d = f_d D_0^d$ up to 3×10^{-3} cm^2 s^{-1} (where $f_d \ll 1$ is the volume fraction of defects and D_0^d the limiting pre-exponential scaling factor of diffusivity along the defective path; refer to Nteme et al. (2023) for more details on this parameter).

In the case of phlogopite, the empirical basis for comparing MD + NEB results with field-calibrated $P-T$ trends in closure behavior and crystallographic defects is far less developed (if at all) than for white micas, precluding straightforward comparison between diffusion estimates retrieved from different contexts, samples, and methods. Limited *in situ* work does exist, however, that constrains the topology (geometry and extent) of ^{40}Ar diffusion in natural mantle phlogopite, notably by Phillips and Onstott (1988), Phillips (1991), Kelley and Wartho (2000), and Wartho and Kelley (2003). These studies mostly dealed with large phenocrysts > 1 mm in size, commonly categorized as xenocrystic or 'antecrystic' macrocrysts originating from the disaggregation of mantle lithologies during kimberlite ascent. These studies empirically established that the diffusive lengthscale for Ar is the grain radius up to grain sizes in excess of 2 mm (see also Camacho et al., 2005). Zoned grains generally display concentric (but irregular) internal ^{40}Ar/^{39}Ar gradients, either as a result of outward loss or external uptake, further indicating that natural ^{40}Ar intragranular transport occurs through the bulk continuum of the lattice rather than via discrete transgranular defects (cracks, extended defects, grain segmentation).

The most comprehensive work on diffusion-induced ^{40}Ar gradients is that by Phillips and Onstott (1988) and Phillips (1991) who documented true 2D age 'maps' along (001), unlike subsequent studies that exclusively relied on simple (1D) core-to-rim radial traverses with limited lateral resolution likely affected by non-ideal ^{40}Ar/^{39}Ar concentric patterns (Kelley and Wartho, 2000; Wartho and Kelley, 2003; Camacho et al., 2005). Quite remarkably, step-heating ^{40}Ar/^{39}Ar analyses of such large crystals consistently yield staircase patterns closely mimicking these internal Ar gradients (cf. in particular Hopp et al., 2008), pointing to the refractory nature and resilience of phlogopite to thermal decomposition in vacuo. Attempts to model these profiles show that volumic ^{40}Ar transport is not purely Fickian, i.e., controlled by inward diffusive gradients imposed by the rim geometry with a single activation energy. 2D layer-parallel ^{40}Ar/^{39}Ar patterns are invariably complex (hat-toped to bell-shaped) and have been interpreted to involve a mosaic of nested sub-grain domains with variable radii of diffusion along (001) (± local extended defects) to explain the more depressed ages commonly found near the rims (Phillips, 1991).

These 2D ^{40}Ar/^{39}Ar patterns are very similar in size and topology to those recently mapped by Nteme et al. (2023) in muscovite. These were suggested to represent diffusion domains broadly concentric, laterally juxtaposed or grading into each other, and preserving older core zones typically 500–400 μm across. FIB–STEM evidence showed these domains to consist of variable-diffusivity zones, including notably lenticular voids and basal partings characterized by high-diffusivity rates scaled by variable ψ_d values (cf. above). Planar features in most respects (length, density, spacing) similar to these defects are documented in the Premier and Swartruggens kimberlite phlogopites (Phillips, 1991) and also in biotite where they are interpreted as Guinier–Preston (GP) zones (Benson Mine biotite, Onstott et al., 1991). GP zones are partial interlayers (rather than voids) coherent with the host lattice, but with slightly differing lattice constants that result in coherency strain due to different octahedral and tetrahedral sheet distortions between layers (Page, 1981). The resulting layer bending (to minimize surface area and match up basal planes locally) may introduce dislocations and sub-grain boundaries along these planar defects, providing the drive to open pores and voids favoring faster (pipe) diffusion along (001) as discussed by Phillips (1991).

In the case of muscovite, the basal defects were inferred to result from inward K ↔ Na interdiffusion during near-solidus fluid–solid reaction with late-stage Na-rich melts or silicate fluids, explaining the patchy development of low-retentive (high-diffusivity) domains across the grains, i.e., not just near the rims but also deep into the interior. No similar structural–substitutional drive has (yet) been proposed to explain planar defects in phlogopites (and neither it is established whether these are common in mantle phlogopite), though GP zones in Benson Mine biotite have been recognized to be more abundant in hydrothermally-reacted grains than in untreated crystals (Onstott et al., 1991), suggesting a possible heterochemical-structural origin as well.

Kimberlitic phlogopites are naturally prone to varying fluid –melt–rock interactions during their lifetime (e.g., Downes et al., 2006). Likewise, their assimilated precursors (mantle xenocrysts) are vulnerable to post-crystallization crystal–melt interactions with low-fraction hydrous melts and fluids in the mantle (Frost, 2006; Casetta et al., 2023a), as testified by magmatic overgrowths and sectorial zoning frequently affecting xenocrystic cores (Giuliani et al., 2016; Dalton et al., 2020). The attending crystal–structural–substitutional modifications are likely to affect the interlayer and the ^{40}Ar diffusion properties in a way similar to muscovite (Nteme et al., 2023), notably via the KBa_{-1} divalent substitution.

Based on the foregoing we suggest that variations in defect density in phlogopite may similarly partition the crystals into Ar–diffusion domains variably concentrated in ~100 nm–sized planar defects. Such partitioning is likely to be irregular (geometrically) and variable (from grain to grain), as indicated by the variable shape of ^{40}Ar/^{39}Ar profiles and 2D contours documented in all mantle phlogopites dated so far. This is the case in particular for the 1D traverses across different grains from the same sample showing similar core and rim ages but highly variable internal gradients (Kelley and Wartho, 2000; Kempton et al., 2001). ^{40}Ar/^{39}Ar variations are also reported between splits from the same mica flakes (Phillips, 1991), indicating that the defective–domainal structure of each grain is unique, as for muscovite (Nteme et al., 2023).

In situ evidence available so far thus suggests that ^{40}Ar diffusion gradients develop in phlogopite like in magmatic muscovite, i.e., via a multi-path diffusion structure consisting of spatially variable domains controlled by their own defect density. This leads to a mosaic of high-diffusivity zones coexisting with (or transitioning smoothly into) low-defect zones preserving near-regular lattice diffusion constants, ideally reflected by our MD + NEB estimates. Dedicated HRTEM and FIB-STEM investigations are clearly needed to document how such internal ^{40}Ar/^{39}Ar domains correlate to structural-compositional defects in diagnostic samples.

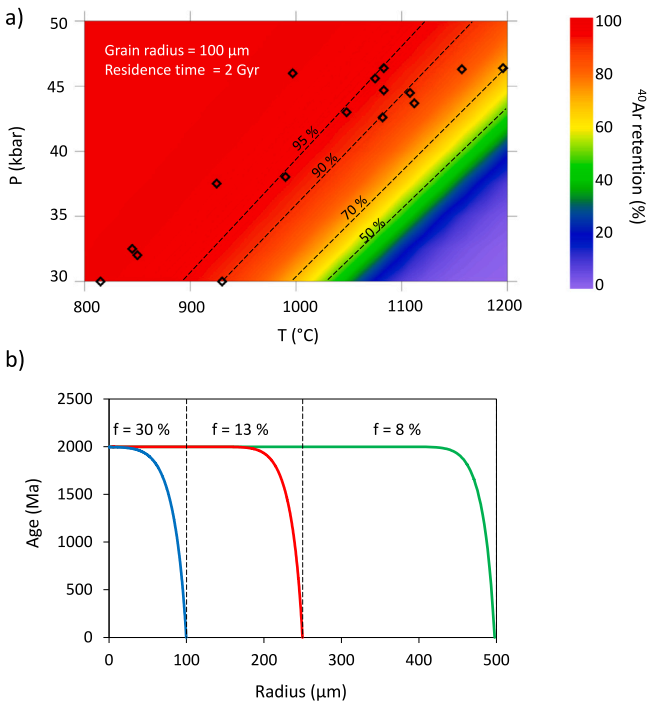

Fig. 8. (a) Pressure–temperature field of radiogenic retention after 2 Gyr residence time for a 100–µm radius phlogopite. Diamond symbols correspond to equilibrium $P-T$ conditions of several xenoliths as reported in Hopp et al. (2008). The red domain basically defines the $P-T$ space of full core retention at the conditions simulated. (b) Diffusion profiles of 100, 250 and 500–µm radius phlogopite grains stalling at 1200 °C and 4.6 GPa for 2 Gyr. Note progressive enlargement of the core-retention domain. f = % bulk integrated loss.

6.2. ^{40}Ar retention behavior at mantle depths: residence time analysis

The preservation of $^{40}Ar/^{39}Ar$ ages older than the kimberlite emplacement age is a primary feature common to almost all xenocrystic kimberlite phlogopites analyzed *in situ* (and often by step-heating as well). These have been interpreted as extraneous contamination by excess ^{40}Ar in the mantle (Phillips, 1991), or as true deep-seated metasomatic ages older than the kimberlite itself (Kelley and Wartho, 2000; Hopp et al., 2008). This extraneous *vs.* radiogenic origin is still debated but both views agree that a high ^{40}Ar partial pressure (P_{Ar}) in excess of the buffering capacity (saturation) of the intergranular fluid phase/melt or the Ar storage capacity of the grain boundary network (Scaillet, 1998; Baxter et al., 2007) is required to maintain and equilibrate the ppm's concentration of ^{40}Ar needed to produce the ages observed. This idea was originally motivated by the available hydrothermal-diffusion data of Giletti et al. (1974) and Giletti and Tullis (1977) precluding then protracted and quantitative ^{40}Ar retention in phlogopite at temperatures characteristic of the sub-continental lithosphere (>1000 °C).

Our revised diffusivity estimates argue in favor of yet another possibility that xenocrystic kimberlite phlogopites (and mantle phlogopites in general) are intrinsically more retentive of ^{40}Ar than suggested by these data. A residence time analysis of the fraction of ^{40}Ar accumulated in a pristine (defect-free and unreacted) phlogopite crystal is provided in Fig. 8a for a range of $P-T$ conditions taken for various Cretaceous kimberlite occurrences intruded inside the late Archean Kaapvaal craton (Hopp et al., 2008). The $P-T$ space is contoured for different fractional retention isopleths ($R_{\%}$) assuming a nominal grain radius of 100 µm with cylinder geometry using the diffusion parameters in Table 4 and a static residence time of 2 Gyr (with the production term included). This radius is taken as the critical core-retention bound characterizing meso- to macrocrystic phlogopite (see below). The retention isopleths would be collectively shifted rightward (to higher–T) by assuming greater grain sizes (Fig. 8b).

It can be seen that near-closed to moderately leaky behavior is predicted for many of the $P-T$ occurrences reported, all plotting above the $R_{70\%}$ retention isopleth. Note that a residence time of t_{res} = 2 Gyr was selected not only to make fully apparent the transitional retention interval between closed behavior (arbitrarily at $R_{99\%}$) and massively leaking systems (~ $R_{50\%}$). Adopting shorter holding times would similarly shift all isopleths rightward, eventually predicting no or only minor effective loss at the considered $P-T$ positions for $t_{res} < 1$ Gyr. More fundamentally, the 2 Ga value corresponds to the difference between the oldest core ages and the kimberlite eruption age observed in nearly all xenocrystic kimberlite phlogopites analyzed *in situ*. It is also close to the putative 2.0–2.5 Ga age of the global primordial kimberlite mantle reservoir that remained isolated with a coherent time-integrated $\epsilon Nd-\epsilon Hf$ lineage from the depleted convective upper mantle until its remobilization, at *ca.* 200–225 Ma, as a result of subduction along the margin of the Pangea supercontinent ('Primitive kimberlites' array, Woodhead et al., 2019).

The calculated $^{40}Ar/^{39}Ar$ age profiles for different grain radii show that the characteristic diffusion penetration distance is about 100 µm at a nominal P = 4.6 GPa (Fig. 8b). This defines the critical size a for which the crystallization age of a 2 Gyr–old phlogopite would remain untouched in the core despite residing and incurring a bulk integrated loss of ~30% at such conditions in the mantle. Larger grains would retain larger isochronous core zones with a bulk loss decreasing with increasing effective radius.

These calculations clearly support the hypothesis that phlogopite may retain primordial argon from its mantle source or reservoir. In real-life samples, such retention properties are potentially mitigated by faster-diffusing conditions associated with the multi-domain structure discussed above (Section 6.1). Still, the fact remains that (*i*) such resetting in the rims is a secondary process post-dating early entrapment, and (*ii*), all core domains retaining older ages are typically bigger than our critical size a = 100 µm (generally in the range 350–450 µm, Phillips and Onstott, 1988; Phillips, 1991), placing them in the high-retention $P-T$ field as long as their primary (undefective) diffusion characteristics are substantially preserved.

6.3. Old–aged cores: excess ^{40}Ar or primordial mantle signature?

The sensitivity calculations above cannot discriminate between a radiogenic *vs.* extraneous origin of the ^{40}Ar trapped at mantle depth. They just predict that any initial or *in situ* produced ^{40}Ar is stably trapped in phlogopite. The kinetic implications in terms of trapping mechanism and inherited mantle ^{40}Ar signature are fundamentally different, however. One consequence of our low diffusion estimates is that radiogenic buildup ($^{40}Ar^{*}$) is bound to contribute a substantial fraction of the total ^{40}Ar budget of any phlogopite residing in the mantle, unless it is soon removed from its source zone after crystallization, or totally reset by local thermal-metasomatic transformations shortly prior to kimberlite ascent. The corollary is that a purely mantle (i.e., exotic or indigenous – instead of radiogenic) origin for the ^{40}Ar found in excess of the age of eruption requires the xenolith phlogopites to have crystallized soon (i.e., certainly not Gyrs) before eruption. Further, a metasomatic (i.e., pre-kimberlite) Ar inheritance to explain the older cores requires primary (syn-crystallization) equilibrium entrapment to affect the core. Secondary (post-crystallization) contamination is indeed excluded since stable incorporation of extraneous ^{40}Ar by diffusive up-take in a pre-existing pristine mica at mantle P is bound to be extremely slow, requiring hundreds (if not thousands) of Myr to achieve equilibrium with the core of grains > 100 µm across.

Homogeneous, near-equilibrium, ^{40}Ar incorporation during (re)crystallization under melt saturation conditions at the liquidus (for kimberlite phlogopite) or fluid saturation conditions (for xenocrystic metasomatic phlogopite) implies crystal growth physics and crystal–

melt/fluid ^{40}Ar partitioning not modeled here. Ar–solid solubility and Ar–fluid/melt partition in the mantle are governed by thermodynamical mixing properties of H_2O–CO_2–Ar– melt systems (Paonita and Martelli, 2007). These combine with physical variables such as interfacial segregation, melt fraction, transmissive timescale, permeability, and grain-boundary sink capacity (e.g., Baxter et al., 2007; Smye et al., 2013) in controlling Ar–melt–solid kinetic interactions during metasomatism and ascent. Published experimental solubility data for Ar in phlogopite are restricted to rather shallow (and narrow) conditions between 350–900 °C at 0.06–1.77 kbar (Jackson et al., 2015), far removed from (and likely inadequate to quantitatively predict) the conditions prevailing in the mantle. Ar solubility data at higher P – T (1, 6, 10 kbar, and 800, 1000, 1100, 1200, and 1300 °C) have been presented in abstract or unpublished form only (Roselieb et al., 1999; Cruz, 2018). These pertain to Ar–pressurized synthetic fluorphlogopite, not to melt nor silicate fluid–mica equilibria, and have yielded widely scattered Henry's Law coefficients between $S_{Ar}^{phl} = 0.002-0.139$ ppm.bar^{-1}. These data are of uncertain applicability since, at such high artificial pressures, Ar may be trapped in pre-existing (or induced) extended defects or micro/nano-inclusions, resulting in anomalously high apparent solubilities.

Independent data for olivine indicate that the compatibility behavior of Ar in mantle phases is complex with competing effects of bulk equilibrium and interface segregation that may reduce Ar–mineral solubility in favor to storage at mineral interfaces (Pinilla et al., 2012), with reduced Ar mobility at dry (melt–free) grain–boundaries (Delon et al., 2019). The situation in the presence of melt or metasomatic fluids is more complex and controlled by miscibility and wetting properties of carbonate-rich melt and aqueous fluids at mineral interfaces (Baxter et al., 2007). The connectivity of CO_2–bearing melts in the mantle is high as indicated by low dihedral angles (<30°) and non-vanishing electrical conductivity measured down to very small melt fractions (Watson et al., 1990; Minarik and Watson, 1995; Gaillard et al., 2019). Ar solubility in these melts is low as determined by recent MD simulations (Desmaele et al., 2020), in contrast to water that has a strong solvation power in carbonate melts (Foustoukos and Mysen, 2015). Water solubility in kimberlite melt have their maximum near 7–9 wt%, as addition of silicate component to carbonatitic melts will decrease the amount of soluble H_2O (Keppler, 2003; Moussallam et al., 2016). These are considered the highest permissible values for the solubilities of these species in the two–component H_2O + CO_2 fluid as mutual interactions of H_2O and CO_2 reduce their saturation content in a combined fluid phase (Kopylova et al., 2007). Also, kimberlite magmas exceeding volatile contents around 10 wt% H_2O are also likely to have phenocryst loads too high (> 50 wt%) to permit their eruption (Kavanagh and Sparks, 2009), and are probably not those sampled at the surface.

This raises the question of the fluid–vapor–solid mixing properties of multi-phase H_2O– CO_2–Ar–melt systems, and the partitioning (and solubility) of Ar in the residual aqueous phase potentially in excess of the fluid saturation limit of the melt (where it is likely to reside). The CO_2 and argon dihedral angles are the highest observed for any volatile fluid composition in most systems examined so far (Holness, 1997), and their well-documented property to form non-wetting fluids has raised the possibility that (the non-polar) argon could, in the aqueous fluid phase, affect fluid–solid interfacial free energies of H_2O–CO_2–Ar mixtures to form isolated pockets at grain-edge triple-junctions at ultra-high pressures (UHP, Scaillet, 1998), an effect supported by experimental data on wetting angle characteristics for pure Ar and H_2O–Ar mixtures in hot-pressed monomineralic aggregates (Holness, 1993; Holness and Graham, 1995).

The overall picture that emerges from these relationships is that 'free' (dissolved) Ar in the pre- or proto-kimberlite mantle would preferentially reside at wetted grain boundary or triple-junctions at very low fluid/melt fractions, but $K_{Ar}^{phl/melt}$ remains largely under-constrained in these systems. Combining these rather disparate Ar–fluid–melt–crystal data has produced Ar partition coefficients from compatible to fully incompatible ($K_{Ar}^{melt/phl} = 0.028-2.8$, Cruz, 2018), like for Ar in mantle olivine and enstatite (Watson et al., 2007; Cassata et al., 2011; Pinilla et al., 2012), illustrating the difficulty of extrapolating these estimates to predict Ar–solid/melt kinetic interactions with any reliability in mantle xenoliths and kimberlites. On top of the lack of properly calibrated $K_{Ar}^{phl/melt}$ is the mere observation that *in situ* ablation studies of texturally-tied ^{40}Ar/^{39}Ar variations, such as documented in other deep-seated rocks (granulites, Maluski et al., 1990), are simply lacking in pristine xenolithic nodules. These are critically needed to provide first-hand constraints on the origin and textural siting of labile ^{40}Ar in real mantle phases.

6.4. Partial ^{40}Ar resetting: ascent-driven diffusive relaxation vs. crystal–melt metasomatic interactions

Elemental zoning is systematic in mantle and liquidus/sub-solidus kimberlite phases as a result of crystal–melt metasomatic interactions and solid-state diffusion during ultra-fast kimberlite ascent to the surface (e.g. Peslier and Luhr, 2006; Peslier et al., 2008; Jollands et al., 2018; Howarth and Gross, 2019). Such re-equilibration profiles have been extensively used to constrain exhumation rates, notably in olivine by Fe–Mg and H diffusion chronometry coupled with $P-T-X$ changes recorded during ascent (Soltys et al., 2020; Abersteiner et al., 2022; Casetta et al., 2023b) and include also ^{40}Ar/^{39}Ar in phlogopite (e.g., Phillips, 1991; Pearson et al., 1997; Kelley and Wartho, 2000; Kempton et al., 2001; Wartho and Kelley, 2003; Downes et al., 2006).

These models assume that ^{40}Ar gradients are produced by disequilibrium relaxation of the initial argon trapped at depth due to instant removal of a high partial mantle P_{Ar} upon decompression and fast ascent to the surface, likely as a consequence of extensive volatile exsolution in the melt due to the drop in thermal compressibility (Phillips, 1991). Physically, a zero-boundary (homogenous Dirichlet boundary) condition is modeled to re-equilibrate the crystals along the upwelling isothermal path, triggering ^{40}Ar diffusive loss into the host kimberlite melt all the way up to the surface. Such isothermal diffusive–relaxation (IDR) models have been simulated at melt temperatures (950–1100 °C) using available ^{40}Ar diffusion data (Giletti et al., 1974; Giletti and Tullis, 1977) to reproduce the bulk loss empirically documented in zoned crystals (between 1–40% loss, depending on grain size). These simulations have returned transit rates between 0.1–4 m s^{-1} for a selection of xenolithic phlogopites from several localities worldwide (Phillips, 1991; Kelley and Wartho, 2000; Wartho and Kelley, 2003). Note that these calculations are unaffected by whether ^{40}Ar in the cores is radiogenic or inherited since it is the collective loss from the initial stock that is modeled (the initial ^{40}Ar is just assumed homogeneous).

While the ascent rates deduced from these models appear to fall in the range of values derived from other diffusion–chronometric systems (and have been used as an independent confirmation thereof, e.g., Costa and Morgan, 2010), they are likely to be wrong in terms of kinetics and relaxation mechanism(s). IDR models invoke purely isochoric–isothermal diffusion to re-equilibrate phlogopite but ignore reversible elastic strain relaxation due to adiabatic–isentropic changes during ascent. These affect the isothermal bulk modulus of phlogopite and loss–retention ^{40}Ar kinetics via ΔV during decompression. With the highest activation volume among all diffusing species used in ascent-rate speedometry, Ar (in phlogopite) possesses the greatest sensitivity to pressure changes during upwelling, a characteristic surprisingly overlooked by previous works given the pressure changes involved. This can be quantitatively appreciated by deriving the corresponding pressure-corrected adiabatic–isentropic loss model (AIL) as follows. The bulk Ar fractional loss after an isothermal pressure drop of duration t at a linear speed $u < 0$ from an initial pressure $P_{initial}$ such that $P(t) = u \cdot t + P_{initial}$ is given by (no source term included):

$$f(\mathrm{Fo}(t)) = 1 - 2\sum_{n=1}^{\infty} \frac{\overline{\beta}_n}{\alpha_n} \exp\left(-\alpha_n^2 \mathrm{Fo}(t)\right) \quad (10)$$

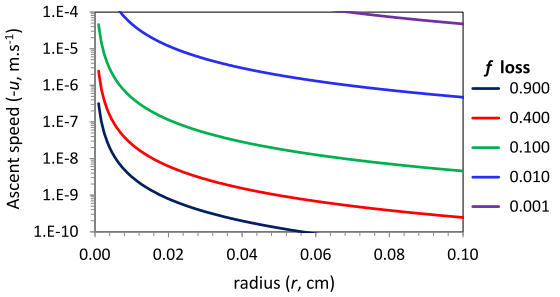

Fig. 9. Adiabatic– isentropic loss plot showing the trade-off between ascent rate and effective diffusion radius for various retention-loss isopleths.

where the weight factors $\overline{\beta}_n$ and eigenvalues α_n depend on the geometry of the system (Gardés and Montel, 2009). $\mathrm{Fo}(t) = (D_T/r^2)\kappa_S(t)$ is the time-integrated Fourier number scaled by the grain radius (r) and the adiabatic–isentropic factor $\kappa_S(t)$ accounting for the decompression-driven increase in diffusivity:

$$\kappa_S(t) = \frac{RT}{u\Delta V}\left[\frac{D_{\text{initial}} - D(t)}{D_T}\right] \tag{11}$$

where D_{initial} is the initial diffusion coefficient at $(P_{\text{initial}};T)$ and D_T is the diffusion coefficient at the reference state taken at zero pressure $(P=0;T)$:

$$D_T = D_0 \exp\left(-\frac{E}{RT}\right) \tag{12}$$

Assuming exhumation up to the surface ($P_{\text{final}} = 0$), we have:

$$\mathrm{Fo} = \frac{1}{r^2}\frac{RT}{u\Delta V}\left[D_{\text{initial}} - D_T\right] \tag{13}$$

Note that this is exactly the standard IDR model when $\Delta V = 0$. On taking the limit $\Delta V \to 0$ one can show that $\kappa_S(t) \to \Delta t = (t_{\text{final}} - t_{\text{initial}})$, from which the isochoric (pressure-free) expression for isothermal loss results: $\mathrm{Fo} = (D_T \Delta t/r^2)$. These fundamental relationships imply $\mathrm{Fo}(\Delta V = 0) \geqslant \mathrm{Fo}(\Delta V \neq 0)$ and show that the IDR end-member model maximizes the apparent loss (and ascent rate) over the AIL formulation for a given upwelling-isothermal path.

These relationships are illustrated using our linear MD–NEB estimates and the diffusion data adopted in previous IDR models (Giletti et al., 1974; Giletti and Tullis, 1977). Ascent rates are by convention negative in our calculations since the driving parameter P decreases during ascent, but our figures directly read off as 'absolute' ascent speeds in m s^{-1} units (i.e., with just the negative sign removed). AIL calculations using the MD–NEB parameters with a cylindrical diffusion geometry for the initial conditions $P_{\text{initial}} = 5$ GPa and $T = 1000$ °C predict phlogopite to remain virtually unaffected by isentropic–adiabatic diffusional relaxation (cf. Fig. 9). Open-system behavior is allowed only for unrealistically low upwelling rates and/or very small diffusion radii (respectively $u < -10^{-4}$ m s^{-1} and $r < 10^{-2}$ cm for a $f_{1\%}$ loss). No loss may otherwise occur during decompression essentially because the pressure-free enthalpy $E_{\text{eff}}^{\text{Ar}\square\square}$ is already very high at 0 GPa (77 kcal mol^{-1}). In contrast, AIL modeling of the diffusion data backing up prior IDR models (Giletti et al., 1974; Giletti and Tullis, 1977), those more likely to approximate the behavior of a defective phlogopite, shows that these are particularly vulnerable to isentropic–adiabatic effects in terms of inferred speed and extent of resetting.

Such kinetic dependence to adiabatic-isentropic effects is illustrated in Fig. 10a via a time-integrated loss analysis for the same starting conditions as above (with $r = 100$ μm) using Giletti's data with variable $\Delta V = \{0, 14, 42\}$ cm^3 mol^{-1}. As can be seen, the effect of increasing ΔV from the limiting IDR case ($\Delta V = 0$) is to 'flip over' the diffusive loss path from convex-up (Fig. 10a) to convex-down (Fig. 10b) in $f(u) \times P$ space. These changes occur as a result of the increasingly delayed opening of the Ar–mica system with rising ΔV, eventually resulting in a

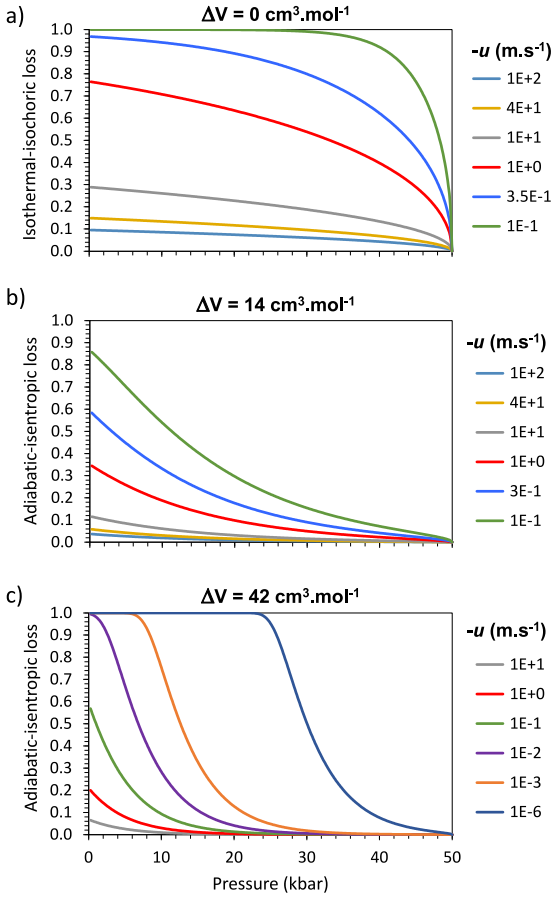

Fig. 10. Fractional loss variation during phlogopite ascent as predicted by the pressure-corrected adiabatic– isentropic loss (AIL) model for different values of activation volume ΔV. See text for discussion.

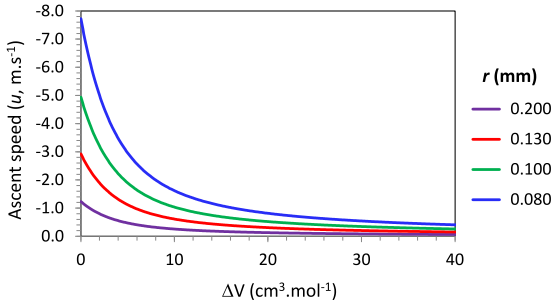

Fig. 11. Isentropic–adiabatic effects on inferred ascent speed for a target loss of $f_{40\%}$ for different effective diffusion radii r. See text for discussion.

distinctly sigmoidal adiabatic–isentropic curve with minimal loss until crystal-lithostatic conditions are reached. This occurs around 20 kbar for $\Delta V = 42$ cm^3 mol^{-1} (Fig. 10c), showing that a deep (mantle) portion of the initial ascending path might not be recorded for high ΔV.

Due to tradeoff between u and ΔV in the denominator of the AIL model (Eq. (13)), the transit time required to produce the same apparent ^{40}Ar loss is considerably longer (and the inferred ascent rate for a given loss correspondingly smaller) relative to the IDR model. The maximum ascent speed is predicted by IDR to be $u_{\max} = -P_{\text{initial}} D_T/r^2/\mathrm{Fo}_{\%}$ (GPa s^{-1}), where $\mathrm{Fo}_{\%}$ is the Fourier number of the associated final loss. For a target loss of $f_{40\%}$ ($\mathrm{Fo}_{40\%} = 3.8 \times 10^{-2}$) from $P_{\text{initial}} = 5$ GPa ($D_{T=1000\ ^\circ\mathrm{C}} = 8.6 \times 10^{-11}$ cm^2 s^{-1}) with $r = 100$ μm, this yields $u_{\max} = -5$ m s^{-1} (Fig. 11). Isentropic–adiabatic effects reduce this value

to -2.5×10^{-1} m s^{-1} at ΔV = 42 cm^3 mol^{-1}, representing a 20−fold reduction from typical IDR estimates (note that the ascent speed is already reduced to a fifth of u_{max} at merely ΔV = 15 cm^3 mol^{-1}). The same calculations for different grain sizes illustrate their strong sensitivity to modest variations in diffusion radius (i.e., a given % error in r results in twice as big a % error in u due to the inverse-squared dependence in Eq. (13)).

To sum up, these calculations reveal that ascent rates derived by previous Ar−IDR modeling are likely variably overestimated due to neglect of isentropic−adiabatic effects. Their constraining power in terms of ascent dynamics is limited to an order-of-magnitude of the process, and possibly worse. More fundamentally, pressure effects predict ascent rates substantially slower than documented by independent mineral-element chronometric pairs with values (0.25−5.0 m s^{-1}) highly unlikely to account for efficient transport of a large cargo of (dense) mantle xenoliths to the surface and the metastable preservation of any diamond from the mantle. This clearly indicates that the extent of ^{40}Ar resetting empirically documented in natural phlogopite is not adequately described by a simple decompression-driven diffusive relaxation process. As discussed in Section 6.1, more realistic options include (pre- or syn-eruptive) sectorially-controlled modification of the rim-to-core crystal structure (by reaction-driven recrystallization or rim overgrowth), concomitant with Ar loss at rates necessarily faster than implied for pure lattice diffusion by MD + NEB.

Almost all mega- to macrocrystic (kimberlite and xenocrystic) phlogopites studied so far are texturally zoned, often featuring a (xenocrystic) core mantled by one (or more) reaction rim(s) or magmatic overgrowth(s) indicating a complex sequence of resorption ± overgrowth ± exchange reactions with the melts(s) (e.g., Downes et al., 2006; Heaman et al., 2006; Osborne et al., 2011; Pokhilenko et al., 2013; Giuliani et al., 2016; Larionova et al., 2016; Kargin et al., 2019; Dalton et al., 2020). All cases cited are systematically associated with complex ^{40}Ar/^{39}Ar release patterns, where available. Temporal and physical modifications associated to such features are likely to be context and sample-specific. This precludes further speculations on ascent-speed dynamics until detailed crystal-structural-compositional SEM + HRTEM observations are coupled with *in situ* ^{40}Ar/^{39}Ar data on samples featuring isotopic and elemental zoning with well-identified growth/interaction episodes with mantle wall rocks and the host melt.

To conclude, we suggest that secondary structural–textural modifications introduced by stoichiometric recombination of xenocrystic and primary kimberlitic phlogopite (either *in situ* or during ascent) are responsible for their characteristic elemental and isotopic zoning. Available textural and grain-scale evidence indicates that ^{40}Ar resetting involves mixed diffusional behavior with spatially and temporally overlapping exchange mechanisms due to metasomatic interactions with external fluids/melts, both leaving highly-retentive cores partly overprinted by variably reacted (and faster Ar-diffusing) defective rims or overgrowths. Extracting ascent rates and kinetic information from the resulting ^{40}Ar/^{39}Ar patterns will remain elusive until more Ar−crystal−chemical data are gathered from coupled SEM−HRTEM and UV-laser studies of critical samples. In such a scenario, the potential for retaining primary (radiogenic or metasomatic) Ar mantle signatures remains very high, though not for the reason foreseen in the past (i.e., high P_{Ar}). Such a characteristic signature more fundamentally reflects intrinsically high Ar retention properties. Next step to disentangle the ^{40}Ar/^{39}Ar chronology of such processes should combine high-resolution sub-grain ^{40}Ar−domain mapping with atomistic modeling as done with muscovite (Nteme et al., 2023).

7. Conclusions

^{40}Ar diffusion in 1M phlogopite has been investigated based on Molecular Dynamics simulations coupled with Nudged Elastic Band and Transition State Theory in order to calibrate the retention properties of this mineral at mantle depths. We find that Ar diffusion rates are several orders of magnitude lower than predicted by previous hydrothermal-diffusion experiments (Giletti et al., 1974; Giletti and Tullis, 1977; Yudin et al., 2021). Crystal-structural thermodynamic PVT relationships retrieved by MD + NEB + TST indicate that the activation volume for Ar diffusion in phlogopite is quite high (42 cm^3 mol^{-1}) and strongly correlated to the reduction in interlayer spacing at increasingly high confining pressure, as documented by compressibility data of natural specimens. Coupled with a high enthalpy and low frequency factor for diffusive motion by divacancy migration along the interlayer (E = 77 kcal mol^{-1}, $D_0 = 6 \times 10^{-4}$ cm^2 s^{-1}), this makes mantle phlogopite virtually immune to diffusive Ar equilibration unless its diffusion structure is altered by structural or compositional modifications during ascent or metasomatism.

Our findings suggest that the ^{40}Ar/^{39}Ar core-rim zoning commonly documented in large xenocrysts, and usually interpreted as diffusive relaxation during kimberlite emplacement, more likely reflect crystal−melt metasomatic interactions prior or during ascent. In particular, there is no need to call upon abnormally high ^{40}Ar pressures at mantle depth to trigger diffusive relaxation by decompression. Adiabatic− isentropic loss modeling predict that the extent of ^{40}Ar resetting (or retention) is strongly modulated by the activation volume and ascent speed rather than pure isothermal diffusive relaxation. Mantle-to-surface transit times predicted from this model are notably lower than inferred by previous ^{40}Ar/^{39}Ar inverse diffusion chronometry assuming isothermal re-equilibration. They indicate that the extent of ^{40}Ar resetting empirically documented most probably results from complex phase interactions with metasomatic agents or the kimberlite melt itself.

The core retention of pre-eruptive ^{40}Ar/^{39}Ar ages remains a largely unsolved but fascinating attribute of zoned mantle phlogopite. Resolving the radiogenic *vs.* trapped signature of this primary component is crucial to deciphering the timing of mantle metasomatism (Buikin et al., 2005) and the potential for tracking recycled Ar in the mantle. As emphasized by these authors, *further investigations of the argon isotopic composition, measured directly in relict intragranular amphibole and intergranular Ba-phlogopite [by laser ablation] should clarify [...] the problem of argon retentivity in K-minerals at mantle conditions*. Almost twenty years later, this has yet to be done.

CRediT authorship contribution statement

Jehiel Nteme: Writing – original draft, Software, Methodology, Formal analysis, Conceptualization. **Stéphane Scaillet:** Writing – original draft, Visualization, Supervision, Methodology, Funding acquisition, Formal analysis, Conceptualization. **Pascal Brault:** Software, Funding acquisition. **Laurent Tassan-Got:** Formal analysis. **Florian Duval:** Data curation.

Declaration of competing interest

The authors declare that they have no known competing financial interests or personal relationships that could have appeared to influence the work reported in this paper.

Data availability

Data are available through Zenodo at https://doi.org/10.5281/zenodo.10592905.

Acknowledgments

Work supported by LABEX, France grant VOLTAIRE (ANR-10-LABX-100-01), the Région Centre grant ARGON, and the EQUIPEX, France grant PLANEX (ANR-11-EQPX-0036). J. Nteme is supported by a post-doctoral grant from the project LABEX-VOLTAIRE. Two anonymous reviewers and Chris Barnes provided thoughtful and perceptive reviews that helped to improve the structure and content.

References

Abersteiner, A., Kamenetsky, V.S., Goemann, K., Golovin, A., Kamenetsky, M., 2022. Olivine in kimberlites: Magma evolution from deep mantle to eruption. J. Petrol. 63, egac055.

Allsopp, H., Roddick, J., 1984. Rb-Sr ^{40}Ar-^{39}Ar age determinations of phlogopite micas from the Pre-Lebombo Group Dokolwayo kimberlite pipe. Spec. Publ. Geol. Soc. South Africa 13, 267–271.

Ammann, M., Brodholt, J., Dobson, D., 2009. DFT study of migration enthalpies in $MgSiO_3$ perovskite. Phys. Chem. Miner. 36, 151–158.

Bailey, S., 1984. Classification and structures of the MICAS. Rev. Mineral 13, 1–12.

Baxter, E.F., Asimow, P.D., Farley, K.A., 2007. Grain boundary partitioning of Ar and He. Geochim. Cosmochim. Acta 71, 434–451.

Brigatti, M.F., Davoli, P., 1990. Crystal-structure refinements of 1M plutonic biotites. Amer. Miner. 75, 305–313.

Buikin, A., Trieloff, M., Korochantseva, E., Hopp, J., Kaliwoda, M., Meyer, H.-P., Altherr, R., 2010. Distribution of mantle and atmospheric argon in mantle xenoliths from the western Arabian Peninsula: Constraints on timing and composition of metasomatizing agents in the lithospheric mantle. J. Petrol. 51, 2547–2570.

Buikin, A.I., Trieloff, M., Ryabchikov, I.D., 2005. ^{40}Ar–^{39}Ar dating of a phlogopite-bearing websterite: Evidence for ancient metasomatism in the subcontinental lithospheric mantle under the Arabian shield? Doklady Earth Sci. 400, 44–48.

Camacho, A., Lee, J.K., Hensen, B.J., Braun, J., 2005. Short-lived orogenic cycles and the eclogitization of cold crust by spasmodic hot fluids. Nature 435, 1191–1196.

Casetta, F., Asenbaum, R., Ashchepkov, I., Abart, R., Ntaflos, T., 2023a. Mantle-derived cargo vs liquid line of descent: Reconstructing the P–T–fO_2–X path of the Udachnaya–East Kimberlite melts during ascent in the Siberian sub-cratonic lithosphere. J. Petrol. 64, egac122.

Casetta, F., Asenbaum, R., Ashchepkov, I., Ageeva, O., Abart, R., Ntaflos, T., 2023b. Ascent rate of the Udachnaya-East kimberlite melts from olivine diffusion chronometry. Earth Planet. Sci. Lett. 619, 118322.

Cassata, W.S., Renne, P.R., Shuster, D.L., 2011. Argon diffusion in pyroxenes: Implications for thermochronometry and mantle degassing. Earth Planet. Sci. Lett. 304, 407–416.

Chheda, T.D., Mookherjee, M., Mainprice, D., Dos Santos, A.M., Molaison, J.J., Chantel, J., Manthilake, G., Bassett, W.A., 2014. Structure and elasticity of phlogopite under compression: Geophysical implications. Phys. Earth. Planet. Inter. 233, 1–12.

Comodi, P., Fumagalli, P., Montagnoli, M., Zanazzi, P., 2004. A single-crystal study on the pressure behavior of phlogopite and petrological implications. Amer. Miner. 89, 647–653.

Costa, F., Morgan, D., 2010. Time constraints from chemical equilibration in magmatic crystals. In: Dosseto, A., Turner, S.P., Orman, J.A. Van (Eds.), Timescales of Magmatic Processes: From Core to Atmosphere. Blackwell Publishing Ltd, pp. 125–159.

Cruz, M.F., 2018. New Applications of Radioisotope Systems in Geologic and Hydrologic Processes (Doctoral Dissertation). Stanford University.

Cygan, R.T., Liang, J.-J., Kalinichev, A.G., 2004. Molecular models of hydroxide, oxyhydroxide, and clay phases and the development of a general force field. J. Phys. Chem. B 108, 1255–1266.

Dahl, P.S., 1996. The crystal-chemical basis for Ar retention in micas: Inferences from interlayer partitioning and implications for geochronology. Contrib. Miner. Petrol. 123, 22–39.

Dahl, P.S., Dorais, M.J., 1996. Influence of $F(OH)_{-1}$ substitution on the relative mechanical strength of rock-forming micas. J. Geophys. Res.: Solid Earth 101, 11519–11524.

Dalton, H., Giuliani, A., Phillips, D., Hergt, J., Maas, R., Matchan, E., Woodhead, J., O'Brien, H., 2020. A comparison of geochronological methods commonly applied to kimberlites and related rocks: Three case studies from Finland. Chem. Geol. 558, 119899.

Delon, R., Demouchy, S., Marrocchi, Y., Bouhifd, M.A., Cordier, P., Addad, A., Burnard, P.G., 2019. Argon storage and diffusion in Earth's upper mantle. Geochim. Cosmochim. Acta 253, 1–18.

Desmaele, E., Sator, N., Guillot, B., 2020. Noble gases in carbonate melts: Constraints on the solubility and the surface tension by molecular dynamics simulation. ACS Earth Sp. Chem. 4, 993–1000.

Downes, P.J., Wartho, J.-A., Griffin, B.J., 2006. Magmatic evolution and ascent history of the Aries micaceous kimberlite, Central Kimberley Basin, Western Australia: Evidence from zoned phlogopite phenocrysts, and UV laser ^{40}Ar/^{39}Ar analysis of phlogopite–biotite. J. Petrol. 47, 1751–1783.

Du, H., Miller, J., 2007. A molecular dynamics simulation study of water structure and adsorption states at talc surfaces. Inter. J. Miner. Process 84, 172–184.

Dunlap, W., 1997. Neocrystallization or cooling? ^{40}Ar/^{39}Ar ages of white micas from low-grade mylonites. Chem. Geol. 143, 181–203.

Fitch, F., Miller, J., 1983. K-ar age of the east peripheral kimberlite at De Beers Mine, Kimberley, RSA. Geol. Mag. 120, 505–512.

Foland, K., 1979. Limited mobility of argon in a metamorphic terrain. Geochim. Cosmochim. Acta 43, 793–801.

Foustoukos, D.I., Mysen, B.O., 2015. The structure of water-saturated carbonate melts. Amer. Miner. 100, 35–46.

Frenkel, D., Smit, B., 2002. Understanding Mol. Simul.: From Algorithms To Applications, second ed. Academic Press, San Diego.

Frost, D.J., 2006. The stability of hydrous mantle phases. Rev. Mineral. Geochem. 62, 243–271.

Gaillard, F., Sator, N., Gardés, E., Guillot, B., Massuyeau, M., Sifré, D., Hammouda, T., Richard, G., 2019. The link between the physical and chemical properties of carbon-bearing melts and their application for geophysical imaging of Earth's mantle. In: Orcutt, B.N., Daniel, I., Dasgupta, R. (Eds.), Deep Carbon: Past to Present. Cambridge University Press, pp. 163–187.

Gardés, E., Montel, J.-M., 2009. Opening and resetting temperatures in heating geochronological systems. Contrib. Miner. Petrol. 158, 185–195.

Giletti, B.J., Hofmann, A., Yoder, H., Yund, R., 1974. Studies in diffusion I: argon in phlogopite mica. In: Geochemical Transport and Kinetics. Carnegie Institution of Washington, Washington, DC, pp. 107–115.

Giletti, B., Tullis, J., 1977. Studies in diffusion, IV. Pressure dependence of Ar diffusion in phlogopite mica. Earth Planet. Sci. Lett. 35, 180–183.

Giuliani, A., Phillips, D., Kamenetsky, V.S., Goemann, K., 2016. Constraints on kimberlite ascent mechanisms revealed by phlogopite compositions in kimberlites and mantle xenoliths. Lithos 240, 189–201.

Hammouda, T., Cherniak, D., 2000. Diffusion of Sr in fluorphlogopite determined by Rutherford backscattering spectrometry. Earth Planet. Sci. Lett. 178, 339–349.

Harrison, T.M., Célérier, J., Aikman, A.B., Hermann, J., Heizler, M.T., 2009. Diffusion of ^{40}Ar in muscovite. Geochim. Cosmochim. Acta 73, 1039–1051.

Harrison, T.M., Duncan, I., McDougall, I., 1985. Diffusion of ^{40}Ar in biotite: Temperature, pressure and compositional effects. Geochim. Cosmochim. Acta 49, 2461–2468.

Hazen, R.M., Finger, L.M., 1978. The crystal structures and compressibilities of layer minerals at high pressure. II. Phlogopite and chlorite. Amer. Miner 63, 293–296.

Heaman, L.M., Creaser, R.A., Cookenboo, H.O., Chacko, T., 2006. Multi-stage modification of the Northern Slave mantle lithosphere: Evidence from zircon-and diamond-bearing eclogite xenoliths entrained in Jericho kimberlite. Canada. J. Petrol. 47, 821–858.

Hernández-Laguna, A., Pérez del Valle, C., Hernández-Haro, N., Ortega-Castro, J., Muñoz-Santiburcio, D., Vidal, I., Sánchez-Navas, A., Escamilla-Roa, E., Sainz-Diáz, C.I., 2019. Compressibility of 2M1 muscovite-phlogopite series minerals. J. Mol. Model 25, 1–16.

Herrero, C., Gregorkiewitz, M., Sanz, J., Serratosa, J., 1987. ^{29}Si MAS-NMR spectroscopy of mica-type silicates: Observed and predicted distribution of tetrahedral Al-Si. Phys. Chem. Miner. 15, 84–90.

Herrero, C., Sanz, J., Serratosa, J., 1985. Tetrahedral cation ordering in layer silicates by ^{29}Si NMR spectroscopy. Solid State Commun. 53, 151–154.

Holness, M.B., 1993. Temperature and pressure dependence of quartz-aqueous fluid dihedral angles: The control of adsorbed H_2O on the permeability of quartzites. Earth Planet. Sci. Lett. 117, 363–377.

Holness, M.B., 1997. Surface chemical controls on pore-fluid connectivity in texturally equilibrated materials. In: Jamtveit, B., Yardley, B.W.D. (Eds.), Fluid Flow and Transport in Rocks: Mechanisms and Effects. Springer, pp. 149–169.

Holness, M., Graham, C., 1995. PTX effects on equilibrium carbonate-H_2O-CO_2-NaCl dihedral angles: Constraints on carbonate permeability and the role of deformation during fluid infiltration. Contrib. Miner. Petrol. 119, 301–313.

Hopp, J., Trieloff, M., Brey, G., Woodl, A., Simon, N., Wijbrans, J., Siebel, W., Reitter, E., 2008. ^{40}Ar/^{39}Ar-ages of phlogopite in mantle xenoliths from South African kimberlites: Evidence for metasomatic mantle impregnation during the Kibaran orogenic cycle. Lithos 106, 351–364.

Howarth, G.H., Gross, J., 2019. Diffusion-controlled and concentric growth zoning revealed by phosphorous in olivine from rapidly ascending kimberlite magma, Benfontein, South Africa. Geochim. Cosmochim. Acta 266, 292–306.

Jackson, C.R., Parman, S.W., Kelley, S.P., Cooper, R.F., 2015. Light noble gas dissolution into ring structure-bearing materials and lattice influences on noble gas recycling. Geochim. Cosmochim. Acta 159, 1–15.

Johnson, L., Phillips, D., 2003. ^{40}Ar/^{39}Ar dating of mantle metasomatism: A noble approach or all hot air?. In: 8th International Kimberlite Conference: Extended Abstracts

Jollands, M.C., Hanger, B.J., Yaxley, G.M., Hermann, J., Kilburn, M.R., 2018. Timescales between mantle metasomatism and kimberlite ascent indicated by diffusion profiles in garnet crystals from peridotite xenoliths. Earth Planet. Sci. Lett. 481, 143–153.

Jónsson, H., Mills, G., Jacobsen, K.W., 1998. Nudged elastic band method for finding minimum energy paths of transitions. In: Classical and Quantum Dynamics in Condensed Phase Simulations. World Scientific, pp. 385–404.

Kaneoka, I., Aoki, K.-I., 1978. ^{40}Ar/^{39}Ar analyses of phlogopite nodules and phlogopite-bearing peridotites in South African kimberlites. Earth Planet. Sci. Lett. 40, 119–129.

Kargin, A., Sazonova, L., Nosova, A., Lebedeva, N., Kostitsyn, Y.A., Kovalchuk, E., Tretyachenko, V., Tikhomirova, Y.S., 2019. Phlogopite in mantle xenoliths and kimberlite from the Grib pipe, Arkhangelsk province, Russia: Evidence for multi-stage mantle metasomatism and origin of phlogopite in kimberlite. Geosc. Front. 10, 1941–1959.

Karki, B.B., Khanduja, G., 2006. Vacancy defects in MgO at high pressure. Amer. Miner. 91, 511–516.

Kavanagh, J.L., Sparks, R.S.J., 2009. Temperature changes in ascending kimberlite magma. Earth Planet. Sci. Lett. 286, 404–413.

Kelley, S., Wartho, J., 2000. Rapid kimberlite ascent and the significance of Ar-Ar ages in xenolith phlogopites. Science 289, 609–611.

Kempton, P., Downes, H., Neymark, L., Wartho, J., Zartman, R., Sharkov, E., 2001. Garnet granulite xenoliths from the Northern Baltic Shield—the underplated lower crust of a Palaeoproterozoic large igneous province? J. Petrol. 42, 731–763.

Keppler, H., 2003. Water solubility in carbonatite melts. Amer. Miner. 88, 1822–1824.

Kopylova, M., Matveev, S., Raudsepp, M., 2007. Searching for parental kimberlite melt. Geochim. Cosmochim. Acta 71, 3616–3629.

Larionova, Y.O., Sazonova, L., Lebedeva, N., Nosova, A., Tretyachenko, V., Travin, A., Kargin, A., Yudin, D., 2016. Kimberlite age in the Arkhangelsk Province, Russia: Isotopic geochronologic Rb–Sr and $^{40}Ar/^{39}Ar$ and mineralogical data on phlogopite. Petrology 24, 562–593.

Loewenstein, W., 1954. The distribution of aluminum in the tetrahedra of silicates and aluminates. Amer. Mineral.: J. Earth Planet. Mater. 39, 92–96.

Maluski, H., Monié, P., Kienast, J., Rahmani, A., 1990. Location of extraneous argon in granulitic-facies minerals: A paired microprobe-laser probe $^{40}Ar/^{39}Ar$ analysis. Chem. Geol.: Isotope Geosc. Sect. 80, 193–217.

Mehrer, H., 2007. Diffusion in Solids: Fundamentals, Methods, Materials, Diffusion-Controlled Processes. Springer Science & Business Media.

Minarik, W.G., Watson, E.B., 1995. Interconnectivity of carbonate melt at low melt fraction. Earth Planet. Sci. Lett. 133, 423–437.

Mitchell, R.H., 1986. Kimberlites: Mineralogy, Geochemistry, and Petrology. Springer Science & Business Media.

Momma, K., Izumi, F., 2011. VESTA 3 for three-dimensional visualization of crystal, volumetric and morphology data. J. App. Crystal. 44, 1272–1276.

Moussallam, Y., Morizet, Y., Gaillard, F., 2016. H_2O–CO_2 solubility in low SiO_2-melts and the unique mode of kimberlite degassing and emplacement. Earth Planet. Sci. Lett. 447, 151–160.

Nteme, Mukonzo J., 2021. Diffusion De L'argon Dans Les Micas: Calibration Empirique Et Simulations Atomistiques (Doctoral Dissertation). University of Orleans.

Nteme, J., Scaillet, S., Brault, P., Tassan-Got, L., 2022. Atomistic simulations of ^{40}Ar diffusion in muscovite. Geochim. Cosmochim. Acta 331, 123–142.

Nteme, J., Scaillet, S., Gardés, E., Duval, F., Nabelek, P., Mottolese, A., 2023. Defect-controlled ^{40}Ar diffusion-domain structure of white micas from high-resolution $^{40}Ar/^{39}Ar$ crystal-mapping in slowly-cooled muscovite. Geochim. Cosmochim. Acta 342, 84–107.

Onstott, T.C., Phillips, D., Pringle-Goodell, L., 1991. Laser microprobe measurement of chlorine and argon zonation in biotite. Chem. Geol. 90, 145–168.

Osborne, I., Sherlock, S., Anand, M., Argles, T., 2011. New Ar–Ar ages of southern Indian kimberlites and a lamproite and their geochemical evolution. Precamb. Res. 189, 91–103.

Page, R., 1981. Partial interlayers in phyllosilicates studied by transmission electron microscopy. Contrib. Miner. Petrol. 75, 309–314.

Paonita, A., Martelli, M., 2007. A new view of the He–Ar–CO_2 degassing at mid-ocean ridges: Homogeneous composition of magmas from the upper mantle. Geochim. Cosmochim. Acta 71, 1747–1763.

Pavese, A., Levy, D., Curetti, N., Diella, V., Fumagalli, P., Sani, A., 2003. Equation of state and compressibility of phlogopite by in-situ high-pressure X-ray powder diffraction. Eur. J. Mineral. 15, 455–463.

Pearson, D., Kelley, S., Pokhilenko, N., Boyd, F., 1997. Laser $^{40}Ar/^{39}Ar$ dating of phlogopites from Southern African and Siberian kimberlites and their xenoliths: Constraints on eruption ages, melt degassing and mantle volatile compositions. Geol. Geof. 1, 100–111.

Peslier, A.H., Luhr, J.F., 2006. Hydrogen loss from olivines in mantle xenoliths from Simcoe (USA) and Mexico: Mafic alkalic magma ascent rates and water budget of the sub-continental lithosphere. Earth Planet. Sci. Lett. 242, 302–319.

Peslier, A.H., Woodland, A.B., Wolff, J.A., 2008. Fast kimberlite ascent rates estimated from hydrogen diffusion profiles in xenolithic mantle olivines from Southern Africa. Geochim. Cosmochim. Acta 72, 2711–2722.

Phillips, D., 1991. Argon isotope and halogen chemistry of phlogopite from South African kimberlites: A combined step-heating, laser probe, electron microprobe and tem study. Chem. Geol.: Isotope Geosc. Sect. 87, 71–98.

Phillips, D., Kiviets, G., Barton, E., Smith, C., Viljoen, K., Fourie, L., 1999. $^{40}Ar/^{39}Ar$ dating of kimberlites and related rocks: Problems and solutions. In: Procedings of the 7th International Kimberlite Conference, Cape. pp. 677–687.

Phillips, D., Onstott, T.C., 1986. Application of $^{36}Ar/^{40}Ar$ versus $^{39}Ar/^{40}Ar$ correlation diagrams to the $^{40}Ar/^{39}Ar$ spectra of phlogopites from Southern African kimberlites. Geophys. Res. Lett. 13, 689–692.

Phillips, D., Onstott, T.C., 1988. Argon isotopic zoning in mantle phlogopite. Geology 16, 542–546.

Pinilla, C., Davis, S.A., Scott, T.B., Allan, N.L., Blundy, J.D., 2012. Interfacial storage of noble gases and other trace elements in magmatic systems. Earth Planet. Sci. Lett. 319, 287–294.

Pokhilenko, L., Alifirova, T., Yudin, D., 2013. $^{40}Ar/^{39}Ar$-dating of phlogopite from mantle xenoliths: Evidence for deep ancient metasomatism of the Siberian craton lithosphere. In: Doklady Earth Sciences. Springer, pp. 309–312.

Rapaport, D.C., 2004. The Art of Molecular Dynamics Simulation. Cambridge University Press.

Reguir, E., Chakhmouradian, A., Halden, N., Malkovets, V., Yang, P., 2009. Major- and trace-element compositional variation of phlogopite from kimberlites and carbonatites as a petrogenetic indicator. Lithos 112, 372–384.

Roselieb, K., Wartho, J., Buttner, H., Jambon, A., Kelley, S., 1999. Solubility and diffusivity of noble gases in synthetic phlogopite: A UV LAMP investigation. Terra Abstr. 4, 368.

Scaillet, S., 1998. K-Ar ($^{40}Ar/^{39}Ar$) geochronology of ultrahigh pressure rocks. In: B.R. Hacker, J.G. Liou (Ed.), When Continents Collide: Geodynamics and Geochemistry of Ultrahigh-Pressure Rocks. Springer, pp. 161–201.

Scibiorski, E., Jourdan, F., Mezger, K., Tohver, E., Vollstaedt, H., 2021. Cryptic excess argon in metamorphic biotite: Anomalously old $^{40}Ar/^{39}Ar$ plateau dates tested with Rb/Sr thermochronology and Ar diffusion modelling. Geochim. Cosmochim. Acta 315, 1–23.

Sharp, T.G., Otten, M.T., Buseck, P.R., 1990. Serpentinization of phlogopite phenocrysts from a micaceous kimberlite. Contrib. Miner. Petrol. 104, 530–539.

Smye, A.J., Warren, C.J., Bickle, M.J., 2013. The signature of devolatisation: Extraneous ^{40}Ar systematics in high-pressure metamorphic rocks. Geochim. Cosmochim. Acta 113, 94–112.

Soltys, A., Giuliani, A., Phillips, D., Kamenetsky, V.S., 2020. Kimberlite metasomatism of the lithosphere and the evolution of olivine in carbonate-rich melts—evidence from the Kimberley kimberlites (South Africa). J. Petrol. 61, egaa062.

Szczerba, M., Derkowski, A., Kalinichev, A.G., Środoń, J., 2015. Molecular modeling of the effects of ^{40}Ar recoil in illite particles on their K–Ar isotope dating. Geochim. Cosmochim. Acta 159, 162–176.

Thompson, A.P., Aktulga, H.M., Berger, R., Bolintineanu, D.S., Brown, W.M., Crozier, P.S., in't Veld, P.J., Kohlmeyer, A., Moore, S.G., Nguyen, T.D., et al., 2022. LAMMPS-A flexible simulation tool for particle-based materials modeling at the atomic, meso, and continuum scales. Comp. Phys. Comm. 271, 108171.

Vysotskii, S., Budnitskii, S.Y., Rasskazov, S., Ignat'ev, A., Velivetskaya, T., Karabtsov, A., 2011. Preservation of radiogenic argon in mantle micas in situ: Dating of deep seated inclusions from the Shavaryn-Tsaram Paleovolcano, Mongolia. In: Doklady Earth Sciences. Springer, pp. 1423–1426.

Wang, K., Lu, X., Brodholt, J.P., 2020. Diffusion of noble gases in subduction zone hydrous minerals. Geochim. Cosmochim. Acta 291, 50–61.

Wartho, J.-A., Kelley, S.P., 2003. $^{40}Ar/^{39}Ar$ ages in mantle xenolith phlogopites: Determining the ages of multiple lithospheric mantle events and diatreme ascent rates in Southern Africa and Malaita, Solomon Islands. Geol. Soc. Lond. Spec. Publ. 220, 231–248.

Watson, E.B., Brenan, J.M., Baker, D.R., 1990. Distribution of fluids in the continental mantle. In: Menzies, M.A. (Ed.), Continental Mantle. Clarendon Press, pp. 111–125.

Watson, E.B., Thomas, J.B., Cherniak, D.J., 2007. ^{40}Ar retention in the terrestrial planets. Nature 449, 299–304.

White, J.A., 1999. Lennard-Jones as a model for argon and test of extended renormalization group calculations. J. Chem. Phys. 111, 9352–9356.

Woodhead, J., Hergt, J., Giuliani, A., Maas, R., Phillips, D., Pearson, D.G., G., Nowell, 2019. Kimberlites reveal 2.5-billion-year evolution of a deep, isolated mantle reservoir. Nature 573, 578–581.

Yudin, D., Murzintsev, N., Travin, A., Alifirova, T., Zhimulev, E., Novikova, S., 2021. Studying the stability of the K/Ar isotopic system of phlogopites in conditions of high T, P: $^{40}Ar/^{39}Ar$ dating, laboratory experiment, numerical simulation. Minerals 11, 192.